

#6  
NSG-5713

710-34-0R

570900  
450.

TRANSITION TO TWO-DIMENSIONAL  
TURBULENT CONVECTION  
IN A RAPIDLY-ROTATING ANNULUS

R.-q. Lin<sup>\*</sup>, F. Busse<sup>\*\*,+</sup> and M. Ghil<sup>•,\*\*</sup>

University of California, Los Angeles, CA 90024, U.S.A.

AI/A/TIS

1988 MAR -8 A 8:05

RECEIVED  
LIBRARY

October 1987

\* Climate Dynamics Laboratory and Department of Atmospheric Sciences, UCLA

\*\* Institute of Geophysics and Planetary Physics, UCLA

+ Theoretical Physics IV, University of Bayreuth, D-8580 Bayreuth, West Germany

Geophys. Astrophys. Fluid Dyn., submitted

(NASA-CR-186436) TRANSITION TO  
TWO-DIMENSIONAL TURBULENT CONVECTION IN A  
RAPIDLY-ROTATING ANNULUS (California Univ.)

45 D

N90-70712

Unclass

00/34 0270900

Abstract

We study a semi-analytical model of convection in a rapidly-rotating, differentially-heated annulus with sloping top and bottom lids. Rapid rotation leads to a preservation of relatively simple, two-dimensional (2-D) structure of the experimentally-observed flow, while temporal complexity increases with the Rayleigh number. The 2-D model exhibits a sequence of bifurcations from steadily-drifting, azimuthally-periodic convection columns, also called thermal Rossby waves, through vacillation and a period-doubling cascade, to aperiodic, turbulent solutions.

Our semi-analytical results match to within a few percent previous numerical results with a limited-resolution 2-D model, and extend these results, due to the greater flexibility of the model presented here. Two types of vacillation are obtained, which we call, by analogy with classical nomenclature of the baroclinic annulus with moderate rotation rates, amplitude vacillation and tilted-trough vacillation. Their properties and dependence on the problem's nondimensional parameters are investigated. The period-doubling cascade for each type of vacillation is studied in some detail.

---

KEY WORDS: Convection, deterministic chaos, rotating annulus, turbulence, vacillation.

## 1. INTRODUCTION

Convection driven by centrifugal buoyancy in a rotating cylindrical annulus is an interesting research topic for a number of reasons. The original motivation for investigating this subject arose from the desire to understand thermal convection in rotating spherical fluid shells and spheres (Busse, 1970), such as planetary cores and deep planetary atmospheres. Convection in the Earth's core and in the outer parts of the major planets shares several basic dynamical properties with the drifting convection columns that can be observed in a rapidly-rotating cylindrical-annulus experiment. There are important physical effects, such as the Lorentz force exerted on the flow by magnetic fields and the effects of fully-developed turbulence, which cannot easily be modelled in laboratory experiments (Ghil and Childress, 1987, Chapters 7-9). But as long as the Coriolis force dominates, the correspondence between planetary-scale features and those observed in the laboratory seems to be closer than usually expected in non-rotating systems.

Further comparison with laboratory experiments is another attraction of the rapidly-rotating annulus problem. In contrast to the classical, baroclinic annulus experiments (Fultz et al., 1959; Hide, 1977; Ghil and Childress, 1987, Chapter 5), the rotation rate of the centrifugally-driven convection experiment is typically very high, such that the centrifugal force becomes comparable to or larger than gravity. Because of the rapid rotation of the annulus, the experimental data are not easily obtainable and the results that have been acquired so far (Busse and Carrigan, 1974; Azouni et al., 1986) need to be extended in order to provide a detailed comparison with the results of nonlinear theories. On the other hand, rapid rotation tends to maintain the two-dimensional (2-D) structure of the flow field, in a manner analogous to large, parallel magnetic fields

in Rayleigh-Bénard convection of an electrically conducting fluid (Libchaber, 1985), while the temporal and 2-D spatial complexity increases markedly with Rayleigh number in both cases.

A third motivation for studying convection in a rapidly-rotating annulus is the important modification of the classical Rayleigh-Bénard problem introduced by the Coriolis force, owing to a rotation vector which is perpendicular to the direction of the effective gravity provided by the centrifugal force. When the end walls bounding the annular fluid domain in the axial direction are parallel, there is actually very little difference between the convection rolls aligned with the axis of rotation in the annulus, and the convection rolls in a horizontal fluid layer heated from below. The Coriolis force is balanced by the pressure and only the thin Ekman layers at the end walls may exert an influence on the dynamics of the rolls or columns.

If, however, the end boundaries are of conical shape such that the height of the annular region in the axial direction varies with distance from the axis, a profound influence of the Coriolis force on the flow becomes noticeable. Instead of stationary convection relative to the rotating frame of reference, drifting columns, also called thermal Rossby waves (Busse, 1986; Or and Busse, 1986), are observed and the critical value of the Rayleigh number for the onset of convection experiences a strong increase. For asymptotically large rotation rates  $\Omega$ , the critical Rayleigh number follows an  $\Omega^{4/3}$ -dependence. Concurrently, the Rayleigh numbers for the onset of higher modes, i.e. those with one or more nodes in the radial dependence, become relatively close to the critical Rayleigh number, while the 2-D structure of the flow field persists. This property opens up the possibility for mixed-mode convection which does not seem to occur, at least not in this particular form, in ordinary Rayleigh-Bénard convection, but does appear in the baroclinic annulus problem with moderate rotation rates (Ghil and

Childress, 1987, Section 5.3).

The secondary and subsequent bifurcations introduced by mixed-mode convection are the subject of the present paper. The semi-analytical treatment follows the outline given by Busse (1986), in collaboration with R.-q. Lin, which will be referred to as B86 in the following. One goal of the analysis is to understand the bifurcation structure of the codimension-2 problem presented by the interaction of the first and the second mode, and to relate it to the results of the numerical computations for the fully-nonlinear problem (Or and Busse, 1986; OB86 in the following).

Numerical computations with many degrees of freedom can provide greater detail in the flow fields and in the fluxes of heat and momentum (e.g., Hathaway and Somerville, 1987). But they do not permit an extensive study of solution dependence on parameters. Hence the possibility of finding solutions of relatively simple equations which reproduce the numerical results, at least qualitatively, is of considerable importance. The dependence of certain features of physical interest, such as the mean zonal-flow speed or the various frequencies of oscillations, on the parameters of the problem can more easily be elucidated in the semi-analytical approach. In addition, new types of solutions are found, as we shall see.

This paper focusses on spatially-periodic solutions. Its main purpose is to validate the semi-analytical approach against OB86, as far as the numerical results went, and to obtain new results on higher bifurcations and on transition to irregular, chaotic flow.

The paper starts with the mathematical formulation of the problem in Section 2. Stationary mixed-mode solutions and their stability properties are analyzed in Section 3. The instabilities introduce time dependences which can no longer be eliminated by the transformation to a drifting frame of reference. Both a

Runge-Kutta integration in time and a Fourier analysis of the time dependence (Urabe, 1967) are used to explore higher bifurcations and transition to turbulence in Section 4. Concluding remarks follow in Section 5.

## 2. MATHEMATICAL FORMULATION OF THE PROBLEM

We consider the fluid flow in a cylindrical annulus heated from the outside, cooled from the inside, and rotating about a vertical axis as shown in Figure 1. We use the gap width  $D$  between the cylindrical walls as length scale,  $D^2/\nu$  as time scale, where  $\nu$  is the kinematic viscosity, and  $\nu\Delta T/\kappa$  as the temperature scale, where  $\Delta T = T_2 - T_1$  is the temperature difference between the walls and  $\kappa$  is the thermal diffusivity of the fluid. Throughout the analysis the small-gap limit will be assumed,  $D \ll r_0$ , where  $r_0$  is the mean radius of the annulus. This allows us to introduce a Cartesian system of coordinates with the  $x$ -coordinate in the radial direction, the  $y$ -coordinate in the azimuthal direction, and the  $z$ -coordinate in the axial direction; in dynamic meteorology and physical oceanography the azimuthal direction is called zonal, and we shall use the two terms interchangeably. The effective gravity induced by the centrifugal force points in the radial direction. An additional component of gravity in the axial direction causes little change in the limit of high rotation rates in which we are interested and turns out to be irrelevant for the following analysis (Busse, 1970). [Fig. 1 near here, please]

Convection sets in as columnar motions, or thermal Rossby waves, when the Rayleigh number  $R$  exceeds a critical value  $R_c$ . Due to the rapid rotation rate, and in accordance with the Taylor-Proudman theorem (e.g., Ghil and Childress, 1987, pp. 14-15), the convective flow is nearly independent of  $z$  and satisfies the geostrophic balance approximately,

$$\underline{v} = \underline{v} \times \underline{k} \psi(x, y, t) + \underline{v}' \quad , \quad (2.1)$$

where  $\underline{k}$  is the unit vector parallel to the axis of rotation and  $\underline{v}'$  denotes the small ageostrophic part of the motion. As has been shown in detail in earlier derivations (B86; Busse and Or, 1986a), the function  $\psi$  and the corresponding deviation  $\theta$  from the basic temperature distribution, which is linear in  $x$ , satisfy the dimensionless equations

$$[\partial_t + \partial_y \psi \partial_x - \partial_x \psi \partial_y] \Delta_2 \psi - \eta^* \partial_y \psi - \Delta_2^2 \psi + R \partial_y \theta = 0 \quad , \quad (2.2a)$$

$$P[\partial_t + \partial_y \psi \partial_x - \partial_x \psi \partial_y] \phi + \partial_y \phi - \Delta_2 \theta = 0 \quad . \quad (2.2b)$$

Here  $\partial_t = \partial/\partial t$ ,  $\Delta_2$  denotes the two-dimensional Laplacian,  $\Delta_2 = \partial_x^2 + \partial_y^2$ , where  $\partial_x^2 = \partial^2/\partial x^2$ ,  $\partial_y^2 = \partial^2/\partial y^2$ , and the three dimensionless parameters  $R, \eta^*$ , and  $P$  are defined by

$$R = \frac{\gamma D^3 \Omega^2 r_0 \Delta T}{\nu \kappa} \quad , \quad \eta^* = \frac{4 \eta_0 D^3 \Omega}{L \nu} \quad , \quad P = \nu / \kappa \quad , \quad (2.2c, d, e)$$

where  $\gamma$  is the coefficient of thermal expansion,  $\Omega$  is the angular velocity of the rotating system,  $L$  is the mean height of the annular region, and  $\eta_0$  is the tangent of the angle  $\chi$  between the conical end boundaries of the annular region and a horizontal plane.  $R$  is a Rayleigh number,  $P$  is the Prandtl number and  $\eta^*$  a parameter measuring the vortex-stretching effect of radial displacements.

The parameter  $\eta^*$  is equivalent to the parameter  $\beta$  of dynamic meteorology and physical oceanography, as in the  $\beta$ -plane approximation, where the meridional dependence of the Coriolis parameter  $f$  is linearized,  $f = f_0 + \beta x$ . This equivalence manifests itself in the Rossby-wave like dynamics of our drifting convective columns, hence the terminology thermal Rossby waves. Although the angle  $\chi$  is assumed to be small,  $\eta^*$  can become arbitrarily large in the limit of vanishing Ekman number  $E$ , where  $E = \nu / \Omega D^2$ . As emphasized in B86, only small changes in the

quantitative aspects must be expected if  $\eta_0$  becomes of order unity, as it usually does in the experimental realizations of the problem.

In the following we study solutions of equations (2.2) subject to the stress-free boundary conditions

$$\psi = \partial_x^2 \psi = \theta = 0 \quad \text{at } x = \pm \frac{1}{2}, \quad (2.3)$$

as explained in the earlier papers mentioned above. For the purposes of the present paper, the conditions (2.3) offer the advantage that simple expressions are obtained for the solutions  $\psi_0^{(n)}$ ,  $\theta_0^{(n)}$  of the linearized form of system (2.2),

$$\psi_0^{(n)} = \sin \pi n (x + \frac{1}{2}) \exp(i\alpha y + i\omega t), \quad \theta_0^{(n)} = i\alpha \psi_0^{(n)} [i\omega P + n^2 \pi^2 + \alpha^2]^{-1}. \quad (2.4)$$

These expressions describe drifting convection columns and solve equations (2.2) after nonlinear advection terms have been neglected, provided the following relationships for  $\omega$  and  $R$  are satisfied:

$$\omega = \omega_0^{(n)} = \frac{-\alpha \eta^*}{(1+P)(n^2 \pi^2 + \alpha^2)}, \quad (2.5a)$$

$$R = R_0^{(n)} \equiv (n^2 \pi^2 + \alpha^2)^3 \alpha^{-2} + \left(\frac{n^* P}{1+P}\right)^2 / (n^2 \pi^2 + \alpha^2). \quad (2.5b)$$

Of particular physical interest are those values of  $\alpha$  for which  $R_0^{(n)}$  reaches a minimum. In the asymptotic case of large  $\eta^*$ , the minimizing value  $\alpha_c^{(n)}$  and the corresponding value  $R_c^{(n)}$  are given by

$$\alpha_c = \eta_p^{1/3} \left(1 - \frac{7}{12} n^2 \pi^2 \eta_0^{-2/3} + \dots\right), \quad R_c^{(n)} = \eta_p^{4/3} (3 + n^2 \pi^2 \eta_p^{-2/3} + \dots), \quad (2.6a, b)$$



where  $\eta_p$  is defined by

$$\eta_p = \frac{\eta^* P}{\sqrt{2(1+P)}} \quad (2.6c)$$

The critical values  $R_c^{(n)} \eta_p^{-4/3}$  associated with distinct values of  $n$  approach each other for large  $\eta^*$ . This fact is the basis for the analytical theory of nonlinear solutions of Eqs. (2.2) which are generated by the interaction of two modes of the form (2.4). The interaction between the modes with  $n = 1$  and  $n = 2$  is of particular interest, since they have the lowest critical values (B86), and the following analysis will be restricted to this case.

Starting with the Ansatz

$$\begin{aligned} \psi_0 = & \left\{ \hat{A}(t) \cos \alpha(y-ct) + \check{A}(t) \sin(\alpha y-ct) \right\} \sin \pi(x+\frac{1}{2}) \\ & + \left\{ \hat{B}(t) \cos \alpha(y-ct) + \check{B}(t) \sin(\alpha y-ct) \right\} \sin 2\pi(x+\frac{1}{2}), \end{aligned} \quad (2.7)$$

we shall try to obtain approximate solutions of equations (2.2) by expanding  $\psi$  in a series

$$\psi = \psi_0 + \psi_1 + \psi_2 + \dots ; \quad (2.8)$$

here  $\psi_1$  represents terms that are quadratic in the amplitudes  $\hat{A}$ ,  $\check{A}$ ,  $\hat{B}$ , and  $\check{B}$ ;  $\psi_2$  represents the cubic terms, and so on. In order to obtain equations for these amplitudes in terms of  $R$  and the average drift rate  $c$  of the solutions, terms up to the cubic order in (2.2) must be taken into account.

The detailed calculations are omitted here. After the representation (2.8) and the corresponding one for  $\theta$  have been inserted into the basic equations (2.2), the solvability conditions for the cubic order are obtained by multiplying Eq. (2.2a) by  $2\psi_0^{(n)*} (Pi\omega_0^{(n)} + n^2\pi^2 + \alpha_c^2)$  and Eq. (2.2b) by  $2R_c^{(n)} \theta_0^{(n)*} (Pi\omega_0^{(n)} + n^2\pi^2 + \alpha_c^2)$  (where the star indicates complex conjugation), averaging the result over the fluid layer and adding the two equations for  $n = 1$  and  $n = 2$ , respectively. Real

and imaginary parts of the equations for  $n = 1, 2$  then give rise to the following four equations for the time dependence of  $\hat{A}(t)$ ,  $\check{A}(t)$ ,  $\hat{B}(t)$ , and  $\check{B}(t)$ :

$$M_1 \frac{d}{dt} \check{A} = [R-R_0^{(1)} - f_0 (\check{A}^2 + \hat{A}^2) - (\hat{B}^2 + \check{B}^2)(g_0 + f_1) - f_2 (\check{B}^2 - \hat{B}^2) + 2f_3 \hat{B}\check{B}] \check{A} \\ + \{Q(R-R_0^{(1)}) - (c-c_0^{(1)})\alpha - \alpha M_1 [c + \alpha^{-1} \omega_0^{(1)} + h_1 (\hat{B}^2 + \check{B}^2) + h_2 (\check{B}^2 - \hat{B}^2) - 2h_3 \hat{B}\check{B}]\} \hat{A}, \quad (2.9a)$$

$$M_1 \frac{d}{dt} \hat{A} = [R-R_0^{(1)} - f_0 (\check{A}^2 + \hat{A}^2) - (\hat{B}^2 + \check{B}^2)(g_0 + f_1) - f_2 (\hat{B}^2 - \check{B}^2) - 2f_3 \hat{B}\check{B}] \hat{A} \\ - \{Q(R-R_0^{(1)}) - (c-c_0^{(1)})\alpha - \alpha M_1 [c + \alpha^{-1} \omega_0^{(1)} + h_1 (\hat{B}^2 + \check{B}^2) + h_2 (\hat{B}^2 - \check{B}^2) + 2h_3 \hat{B}\check{B}]\} \check{A}, \quad (2.9b)$$

$$M_2 \frac{d}{dt} \check{B} = [R-R_0^{(2)} - g_0 (\check{B}^2 + \hat{B}^2) - (\check{A}^2 + \hat{A}^2)(f_0 + g_1) - g_2 (\check{A}^2 - \hat{A}^2) + 2g_3 \hat{A}\check{A}] \check{B} \\ + \{Q(R-R_0^{(2)}) - (c-c_0^{(2)})\alpha - \alpha M_2 [c + \alpha^{-1} \omega_0^{(2)} + k_1 (\hat{A}^2 + \check{A}^2) + k_2 (\check{A}^2 - \hat{A}^2) - 2k_3 \hat{A}\check{A}]\} \hat{B}, \quad (2.9c)$$

$$M_2 \frac{d}{dt} \hat{B} = [R-R_0^{(2)} - g_0 (\check{B}^2 + \hat{B}^2) - (\check{A}^2 + \hat{A}^2)(f_0 + g_1) - g_2 (\hat{A}^2 - \check{A}^2) - 2g_3 \hat{A}\check{A}] \hat{B} \\ - \{Q(R-R_0^{(2)}) - (c-c_0^{(2)})\alpha - \alpha M_2 [c + \alpha^{-1} \omega_0^{(2)} + k_1 (\hat{A}^2 + \check{A}^2) + k_2 (\hat{A}^2 - \check{A}^2) + 2k_3 \hat{A}\check{A}]\} \check{B}. \quad (2.9d)$$

The constants  $f_0$ ,  $g_0$  are given by

$$f_0 = \frac{P^2 \alpha^2 (\pi^2 + \alpha^2)}{8[\omega_0^{(1)2} P^2 + (\pi^2 + \alpha^2)^2]}, \quad g_0 = \frac{P^2 \alpha^2 (4\pi^2 + \alpha^2)}{8[\omega_0^{(2)2} P^2 + (4\pi^2 + \alpha^2)^2]} \quad (2.10)$$

The other constants are given by lengthy expressions which the authors will happily provide upon request.

In the next section we consider steady solutions of Eqs. (2.9) and analyze their stability. In Section 4 a numerical analysis of time-dependent solutions will follow.

### 3. STEADILY DRIFTING CONVECTION COLUMNS

The simplest solutions of Eqs. (2.9) are the "pure" solutions

$$\hat{A}^2 + \hat{A}^2 = (R - R_0^{(1)}) f_0^{-1}, \quad c = -\omega_0^{(1)} / \alpha, \quad \hat{B} = \check{B} = 0, \quad (3.1a)$$

and

$$\check{B}^2 + \check{B}^2 = (R - R_0^{(2)}) g_0^{-1}, \quad c = -\omega_0^{(2)} / \alpha, \quad \hat{A} = \check{A} = 0. \quad (3.1b)$$

Any further restriction on  $\hat{A}, \check{A}$  or on  $\hat{B}, \check{B}$  is precluded by the translational invariance in the  $y$ -direction of the basic equations (2.2). Higher-order terms for the solutions (3.1) have been evaluated by Busse and Or (1986a).

In the present context the "mixed" solutions are of primary interest. In setting  $\hat{A} = 0$ , we break the symmetry of  $\hat{A}$  and  $\check{A}$  imposed by the translational invariance and obtain

$$\check{A}^2 = [(f_1 + f_2 \cos 2\chi + f_3 \sin 2\chi)(R - R_0^{(1)}) + g_0 (R - R_0^{(2)})] N^{-1}, \quad (3.2a)$$

$$\hat{B}^2 + \check{B}^2 = [(g_1 + g_2 \cos 2\chi + g_3 \sin 2\chi)(R - R_0^{(2)}) + f_0 (R_0^{(2)} - R)] N^{-1}, \quad (3.2b)$$

where  $\chi$  and  $N$  are defined by

$$\tan \chi \equiv \hat{B} / \check{B}, \quad N \equiv (g_0 + f_1 + f_2 \cos 2\chi + f_3 \sin 2\chi)(f_0 + g_1 + g_2 \cos 2\chi + g_3 \sin 2\chi) - g_0 f_0. \quad (3.3a, b)$$

The drift rate  $c$  and the relative phase  $\chi$  are determined by the equations

$$c + \omega_0^{(1)} / \alpha = (k_1 - k_2 \cos 2\chi + k_3 \sin 2\chi) (\hat{B}^2 + \check{B}^2), \quad (3.4a)$$

$$c + \omega_0^{(2)} / \alpha = (k_1 + k_2 \cos 2\chi + k_3 \sin 2\chi) \check{A}^2. \quad (3.4b)$$

The results of the amplitude expansion to second order for the mixed-mode solution agree well with the numerical results obtained by OB86. In the presence of nonlinear interactions between multiple waves, OB86 called this the mean-flow solution, since it is characterized by a strong mean zonal flow, induced in their calculations entirely by the convection (compare also Hathaway and Somerville, 1987, where convection reinforced an imposed zonal jet). The zonal-flow component represents a differential rotation, or mean shear, anti-symmetric about the midplane of the small gap. There are in fact two such solutions (B86), differing by a sign, and this fact affects the nature of bifurcations leading to the pair of mean-flow solutions. Figures 2a and 2b, which refer to  $\eta^* = 700$  and  $\eta^* = 1500$ , respectively, show how the mean-flow instability threshold, defined in terms of  $(B-B_c)/B_c$ , varies with  $\alpha$ . Here  $B = RP$  is the buoyancy parameter, and  $\eta^* = 0(10^3)$  corresponds to planetary applications, allowing for an eddy viscosity  $0(10^6 \text{ m}^2/\text{s})$  (OB86). The curves in panels (a) and (b) of this figure agree so closely with those computed numerically by Or (1985, Figures 11 and 20) that we have refrained from reproducing here the latter.

[Fig. 2 near here, please]

We have also found a solution not obtained in OB86. Figure 3 shows bifurcation diagrams as plots of the amplitude versus the buoyancy parameter  $B$ . The numerical method of OB86 gave only the successive bifurcations shown in Fig. 3a. We call this bifurcation tree Solution I. The phase shift between the two waves in Solution I is large,  $\chi = \pm \frac{2\pi}{3}$ . The bifurcations of the new solution, which we call Solution II, are shown in Fig. 3b. The phase shift in Solution II is small,  $\chi = \pm \frac{\pi}{12}$ , and this solution arises at a slightly higher critical value of  $R$ ,  $R'_1 = 30810 > R_1 = 30680$  (at  $\alpha = \alpha_c = 9.37$ ) than Solution I.

[Fig. 3 near here, please]

The two mixed-mode solutions, related by a simple symmetry, appear as a single branch in the bifurcation diagrams of Figures 3a,b, which show only the absolute values  $|A|$  and  $|B|$  of  $A^2 = \hat{A}^2 + \check{A}^2$  and  $B^2 = \hat{B}^2 + \check{B}^2$ . But the existence of the pair is reflected in the fact that the mixed-mode branch is perpendicular to the pure-solution branch from which it emerges (shown as the branch  $(A = A_p, B = 0)$  for Solution I and the branch  $(A = 0, B = B_p)$  for Solution II), at the bifurcation point. This reflects the pitchfork-type of bifurcation involved, imposed by the symmetry of the pair (Guckenheimer and Holmes, 1983, Section 3.4; see also Ghil and Childress, 1987, Figure 5.8, point B, for a similar situation in the classical, baroclinic annulus).

The stability of the mixed-mode solution branches  $(A_m, B_m)$  depends on the sign of  $N$ , Eq. (3.3b). An analysis analogous to that of Busse and Or (1986b) for ordinary Rayleigh-Bénard convection shows that these solutions are stable when  $N > 0$ . In Figure 4 the curve  $N = 0$  is shown in the plane of Prandtl number  $P$  and geometric vortex-stretching number  $\eta^*$ . Prandtl numbers near 1.0 are realistic for the atmospheres of the outer planets, and for the laboratory experiments cited in Section 1.

[Fig. 4 near here, please]

The analysis giving the neutral curve in Figure 4 is based on an asymptotic expansion valid at the point of onset of convection  $R = R_1$ . It gives therefore the actual stability of mixed solutions only in the limit of  $\eta^* \rightarrow \infty$ . Indeed, comparison of Figures 2b and 2d, valid for  $\eta^* = 1500$ , with 2a and 2c, for  $\eta^* = 700$ , shows that the successive bifurcations tend to collapse into  $R_1$  as  $\eta^*$  increases, for both Solution I (Figures 2a, b; see also B86, OB86) and Solution II (Figures 2c, d).

For lower values of  $\eta^*$ , higher-order correction terms are necessary, and for  $\eta^* \rightarrow 0$  the analysis breaks down. An excellent review of multiple bifurca-

tions for competing instabilities appears in Couillet and Spiegel (1983), and the theory works clearly quite well for the high values of  $\eta^*$  in which we are interested. The validity of its application to the lower rotation rates of the classical, baroclinic annulus appears unfortunately more questionable.

#### 4. TIME-DEPENDENT SOLUTIONS

##### 4a. Bifurcation structure

Part of the attraction of the rapidly-rotating annulus, as mentioned already in the Introduction, is that complex temporal behavior can be studied in the context of spatially 2-D, and hence analytically simple, structures. Time-dependent solution branches, associated with the two stationary mean-flow solutions discussed above, emerge. We still call the corresponding branches Solutions I and II, respectively: the corresponding phase shifts  $\chi^I$  and  $\chi^{II}$  now vary with time, but  $\chi^I(t) \gg \chi^{II}(t)$  for all times and for all parameter values we investigated.

Figure 5 shows the successive bifurcations of Solution I (left part of the figure) and Solution II (right part), as a function of the buoyancy parameter  $B$ , for  $P = 1.0$  and  $\eta^* = 700$ . The period  $T$  of the first oscillatory instability is rationally unrelated to the period of propagation  $2\pi/\omega$  of the thermal Rossby wave, for almost all parameter values. Hence the whole regime of flow associated with the period  $T$  and its multiples (see below) can be termed *vacillating*, by analogy with the classical, baroclinic annulus situation (Hide, 1977; Ghil and Childress, 1987, Sec. 5.3). The nature of the vacillation in the zonally-periodic waves of mixed mode will be studied in some detail in Section 4b.

[Fig. 4 near here, please]

A period-doubling cascade, all the way to aperiodic, chaotic or turbulent behavior, is in evidence for both solution branches. The ratios

$$\delta_n = \frac{B_n - B_{n-1}}{B_{n+1} - B_n} \quad (4.1)$$

are known to converge to a value  $\delta \cong 4.67$  (Feigenbaum, 1984). Using the transition to aperiodic behavior as  $B_{n+1}$ , we have the limiting value  $\delta_n \cong 4.78$  for Solution II and  $\delta_n \cong 4.09$  for Solution I. The best experimentally-determined value, for Rayleigh-Bénard convection in liquid helium constrained by a magnetic field, is  $\delta_n \cong 4.4$  (Libchaber, 1985).

Periodic windows within the aperiodic regime beyond transition are part of the full Feigenbaum scenario (Kadanoff, 1983). They have also been observed in numerical studies of simple models of large-scale atmospheric flow (Pedlosky and Frenzen, 1980; Legras and Ghil, 1983). The periods associated with these windows are  $(2k+1)T$ , where  $T$  is the basic period. For Solution I, one observes a period of  $3T_1 \cong 0.66$  at  $B = 39719.97$  and  $5T_1 \cong 1.1$  at  $B = 39721.66$ . For Solution II, periods of  $3T_2 \cong 0.42$  and  $7T_2 \cong 0.98$  are observed at  $B = 40375.43$  and  $B = 40383.11$ , respectively.

The reappearance of a steady-state solution for larger values of the parameter is unrealistic. It is usually an artifact of the low-order truncation (Ghil and Childress, 1987, Section 5.3). Such a spurious "re-simplification" was already encountered by Lorenz (1963b) in a study, similar to the present one, of the classical annulus experiments. We note that, for Solution I, good agreement with the numerical results of OB86 is obtained for  $B < 39725.33$ .

Figures 6a and 6b survey the structure of Solutions I and II in the  $(B-\eta^*)$  plane over the region which we have studied. Solid lines in Figure 6a separate, from lower right to upper left, regions of pure-mode steady states, simply-periodic, multiply-periodic ( $2T$  to  $16T$ ) and aperiodic solutions. Lines in the Figure 6b separate regions of steady state, symmetric simply-periodic, asymmetric simply periodic, multiply-periodic ( $2T$  to  $16T$ ) and aperiodic solu-

tions for the first band. A second region of vacillating solutions is seen in the upper left-hand corner of the figure. An expanded view of the rectangular region near  $\eta^* = 700$ ,  $B = 3.8 \times 10^4$  is shown in the insets in the lower right-hand corner of Figures 6a, b. Transitions between 2T-, 4T-, 8T-, and 16T-periodic solutions are shown in these insets.

[Fig. 6 near here, please]

Figure 7 shows the B-dependence of frequency for solution branches I and II. The solid lines represent Solution I and the dashed lines Solution II. The frequency of Solution II is much higher than the frequency of Solution I for comparable states throughout the whole period-doubling process.

[Fig. 7 near here, please]

The frequencies of each solution are exactly halved at each bifurcation point. Between pairs of period-doubling points, the frequencies of each solution increase slightly. One expects nonlinear oscillators to have amplitude-dependent and/or parameter-dependent frequencies, whether the period has doubled or not. Still, it does not seem to be widely noticed that the "doubled" period will in general only be approximately double the period observed at lower values of the bifurcation parameter (cf. Legras and Ghil, 1983).

The thresholds of vacillating instability for Solutions I and II are plotted in Figure 8 as the critical buoyancy number versus the azimuthal wavenumber  $\alpha$ . The cases shown in Figure 8a and 8b are for Prandtl number  $P = 0.3$  and  $P = 1.0$ , respectively, with  $\eta^* = 700$ . The solid lines represent Solution I and the dashed lines represent Solution II.

[Fig. 8 near here, please]

From Figure 8, we can first see that both the mean-flow and vacillating instabilities of Solution I always appear earlier than the corresponding instabilities of Solution II as the buoyancy number increases. Secondly, the



mean-flow instability occurs for lower  $B$  than the vacillating instability in Solution I as long as the Prandtl number is large (Fig. 8b); this is true of Solution II independently of  $P$  (Figures 8a and 8b). Third, when  $P = 0.3$  and the wave number  $\alpha$  is large, the mean-flow instability boundary of Solution I is lower than the vacillating instability boundary. However, the two boundaries gradually approach each other as  $\alpha$  decreases. They cross at the critical point of the vacillating instability boundary ( $\frac{\partial B}{\partial \alpha} = 0$ ,  $\frac{\partial^2 B}{\partial \alpha^2} > 0$ ). As  $\alpha$  continues to decrease, the boundary of the mean-flow instability occurs at greater  $B$  than the boundary of the vacillating instability, and the distance in  $B$  between the two boundaries increases. All results for Solution I are in total agreement with those for the numerical model of OB86 (Figures 7c, d).

Figures 9a and 9b show the relative position of the mean-flow and vacillating instability boundary of Solutions I and II, respectively, on a graph of  $B$  against  $P$ . The two boundaries cross at  $P \approx 0.2$  and  $P \approx 2.9$  for Solution I and the vacillating instability occurs at larger  $B$  than the mean-flow instability for  $P$  between these two values (Figure 9a). This also agrees well with the numerical results obtained by OB86. For Solution II (Figure 9b), the relative positions of the two stability-threshold curves are the same, both curves are somewhat higher (larger  $B$  for same  $P$ ), the crossover points are  $P \approx 0.6$  and  $P \approx 2.3$ , and the downturn in the vacillation threshold at low  $P$  is not as pronounced as in Solution I.

[Fig. 9 near here, please]

#### 4b. Solution properties

To ascertain the reliability of our numerical results for time-dependent solutions, we compare next two methods of solving Eqs. (2.9) for a simply-periodic, vacillating solution. Figure 10a shows the absolute amplitudes of the first (solid) and second (dashed) modes in the streamfunction of Solution

II, as functions of time, using a fourth-order Runge-Kutta method. Figure 10b shows the variation of the same two modes as calculated by a Fourier-decomposition method (Urabe, 1967, pp. 225-228) in which the time dependence of a periodic solution is projected onto the fundamental period and its harmonics, solving for the undetermined coefficients by a Newton-Raphson method. After adjusting for the arbitrary phase of the vacillation, the two solutions differ by only a few percent. The Fourier-decomposed solution is, by construction, exactly periodic, while the Runge-Kutta solution shows very slight, bounded deviations from periodicity.

[Fig. 10 near here, please]

The power spectrum of Solution II, using both methods, is shown in Figure 11. Panels (a) and (c) show the simple solution ( $B = 38893$ ), while (b) and (d) show the solution after period doubling ( $B = 39156$ ). The power spectra for the same solution computed by the two different methods agree exactly in the position of the peaks and quite well in their amplitude. The largest peaks in the simple solution (panels (a) and (c)), represent the fundamental period; the smaller peaks are harmonics. After period doubling (panels (b) and (d)), the fundamental peak and its harmonics are accompanied also by a peak at half the main frequency, with amplitude intermediate between the fundamental and its first harmonic.

[Fig. 11 near here, please]

Figure 12 shows the time evolution for streamfunction amplitudes of modes 1 and 2 in Solution II, as a function of buoyancy number. The solution is simply-periodic in panel (a) ( $B = 38893$ ), it has undergone periodic doubling in panel (b) ( $B = 40000$ ), period quadrupling in panel (c) ( $B = 40350$ ) and it is aperiodic in panel (d) ( $B = 40375$ ). The slight distortion of the solution in the time domain as it undergoes period doubling in the frequency domain (Figure

11) is quite striking. The period of the vacillation increases from 0.15 to 0.28 and then from 0.55 to infinity as the buoyancy number increases.

[Fig. 12 near here, please]

Figure 13 shows the phase plane of kinetic energy,  $E$  vs.  $dE/dt$ , for Solution I (panel (a)) and Solution II (panel (b)). Figures 14a and 14b show the corresponding phase planes for the velocity components,  $u$  vs.  $v$ .

[Figs. 13 and 14 near here, please]

The features of the successive bifurcations are clearly apparent in these four figures. For Solution I, with the large phase shift between modes (Figures 13a and 14a), transition occurs from (i) the simply-periodic vacillation, to (ii) period doubling, (iii) period quadrupling, through (iv) an  $8T$ -periodic solution to (v) an aperiodic solution. For Solution II, with the small phase shift (Figures 13b and 14b), the transition occurs from (i) the symmetric simply-periodic vacillation to (ii) the asymmetric one (best visible in Figure 14b), through (iii) period doubling and (iv) quadrupling, on to (v) an  $8T$ -periodic and (vi) an aperiodic solution.

A Poincaré section through the solution orbits in the system's four-dimensional (4-D) phase space is obtained as follows: The 3-D "hyperplane"  $\arctan A/B = \pi/3$  is used as a surface of section. The points of intersection between the one-dimensional (1-D) trajectory and this 3-D surface are then projected onto the 2-D (A,B)-plane, leading to the Poincaré maps in Figure 15. Lorenz (1984) has used a somewhat different approach for the detailed study of a strange attractor's local structure in 4-D space by intersections with a 2-D plane.

[Fig. 15 near here, please]

Our main purpose here is the study of the successive stages of transition from thermal Rossby waves, via mixed-mode mean-flow solution, vacillation and

period-doubling cascade to chaotic flow. The stage in the period-doubling cascade is clearly indicated by the number of points in the Poincaré maps of Figure 15,  $n$  points for an  $nT$ -periodic solution. While true aperiodicity cannot be inferred conclusively from any numerical solution of finite length, the difference between Figures 15a(iv) and 15a(v) for Solution I, and between Figures 15b(vi) and 15b(v) for Solution II, is very suggestive of a strange attractor having replaced the  $16T$ -periodic limit cycle, as indicated in Figures 5, 6 and 12-14.

Successive "snapshots" on the streamfunction fields for Solution I and II during one full simple period are shown in Figures 16a and 16b, respectively. A single vertical column appears between the two side walls at  $x = -0.5$  and  $x = 0.5$ . Because the vertical column moves in the azimuthal direction  $y$  with speed  $c$ , we have allowed the coordinate system to move with the same speed, making  $c = 0$ .

[Fig. 16 near here, please]

The periods in Figures 16a and 16b are slightly different, and these periods change with  $B$  as indicated in Figure 7. The largest difference between the two figures, however, is in the asymmetric nature, and stronger vacillation, of the convection columns in panel (b).

Solution I exhibits what is called *amplitude vacillation* in the more slowly rotating, classical annulus: the maximum range of the (nondimensional) streamfunction varies between 25 units and 35 units, with little change in tilt or general shape. Solution II on the other hand shows *shape* or *tilted-trough* vacillation, with a slightly smaller relative change in amplitude, but a pronounced oscillation between forward and reverse tilt of the waves.

It is interesting that in the annulus with moderate rotation rates, barotropic effects predominate in shape vacillation, while baroclinic effects are more involved in amplitude vacillation (Pfeffer and Chiang, 1967; Ghil and

Childress, 1987, Sec. 5.5). This seems to agree with the large phase shift between waves in our Solution I, and the almost vanishingly-small shift in Solution II. The analogies need to be analyzed further, along the lines of B86 and Busse and Or (1986a).

## 5. CONCLUDING REMARKS

High rotation rates and the accompanying Taylor-Proudman effect in a differentially-heated annulus with sloping top and bottom walls lead to nearly two-dimensional (2-D) drifting convection columns. A semi-analytic 2-D model was first proposed by Busse (1986, referred to as B86 throughout our paper) to study a sequence of bifurcations in the behavior of these columns, while Or and Busse (1986, OB86 throughout) obtained partial results on the first few bifurcations with a numerical 2-D model of limited resolution.

Using the semi-analytic model, we pursued the bifurcation sequence from steadily-drifting, azimuthally-periodic columns through vacillation and a period-doubling cascade all the way to temporal aperiodicity or deterministic chaos. In ordinary Rayleigh-Bénard convection between parallel plates and in the differentially-heated annulus with moderate rotation rates, higher temporal complexity is only attained through three-dimensional (3-D) motions of considerable spatial complexity (Buzyna et al., 1984; Hide, 1977; Krishnamurti, 1973; Libchaber, 1985). Thus the classical studies of transition to deterministic chaos using semi-analytic 2-D models in these two problems (Lorenz, 1963a,b) serve as qualitative metaphors, rather than as quantitative guide posts for the observed bifurcation sequence. The rapidly-rotating device, on the other hand, provides hope that our semi-analytic 2-D results are realistic.

All the features of our results that could be tested against the numerical ones of OB86, such as stability thresholds as a function of parameters (Figures

2 and 8), agree to within a few percent, at worst. The results of OB86, in turn, seemed to be in reasonable agreement with experimental results (Azouni et al., 1986; Busse and Carrigan, 1974). In addition to the amplitude vacillation of OB86 (Solution I here, Figure 16a), we have discovered a tilted-trough vacillation (Solution II, Figure 16b), which has frequencies higher than the previous one by about 50% throughout the period-doubling cascade (Figure 7). The experimental and numerical verification of this tilted-trough vacillation in the rapidly-rotating annulus is an immediate suggestion for future work.

High rotation rates, aside from imposing a 2-D structure even to temporally-complex flows, also cause the successive bifurcations to accumulate near the critical Rayleigh number value for the onset of convection. This effect is analogous to that of low Prandtl number in ordinary convection (Krishnamurti, 1973). The accumulation of bifurcation points is an advantage for the analysis of competing instabilities by averaging and unfolding methods (Arnold, 1983, Secs. 33-35; Couillet and Spiegel, 1983; Guckenheimer and Holmes, 1983, Ch. 7). But it makes the careful experimental study of the competing instabilities more difficult. Hence verification of the present results using a semi-analytic model with a larger number of modes might be the next step on the road to understanding the transition to 2-D turbulence in a rapidly-rotating, differentially-heated annulus.

#### Acknowledgements

Figure 7 and the accompanying analysis were motivated by two discussions of one of us (M.G.) with John E. Hart, concerning unpublished work of Richard L. Pfeffer on period doubling in the annulus with moderate rotation rates and with bottom topography. This work was supported by NASA Grant NAG-5713 and by NSF Grant ATM 86-15424. B. Gola typed the manuscript and K. Mantrelli drew the figures.

### References

- Arnold, V. I., *Geometrical Methods in the Theory of Ordinary Differential Equations*, Springer-Verlag, New York/Heidelberg/Berlin, 334 pp. (1983).
- Azouni, A., Bolton, E. W., and Busse, F. H., "Experimental study of convection columns in a rotating cylindrical annulus," *Geophys. Astrophys. Fluid Dyn.*, **34**, 301-317 (1986).
- Busse, F. H., "Thermal instabilities in rapidly rotating systems," *J. Fluid Mech.* **44**, 441-460 (1970).
- Busse, F. H., "Asymptotic theory of convection in a rotating cylindrical annulus," *J. Fluid Mech.* **173**, 545-556 (1986).
- Busse, F. H., and Carrigan, C. R. "Convection induced by centrifugal buoyancy," *J. Fluid Mech.* **62**, 579-592 (1974).
- Busse, F. H., and Or, A. C., "Convection in a rotating cylindrical annulus: thermal Rossby waves," *J. Fluid Mech.* **166**, 173-187 (1986a).
- Busse, F. H., and Or, A. C., "Subharmonic and asymmetric convection rolls," *Z. angew. Math. Phys.*, **24**, 259-271 (1986b).
- Buzyna, G., Pfeffer, R. L., and Kung, R., "Transition to geostrophic turbulence in a rotating differentially heated annulus of fluid," *J. Fluid Mech.*, **145**, 377-403 (1984).
- Coullet, P. H., and Spiegel, E. A., "Amplitude equations for systems with competing instabilities", *SIAM J. Appl. Math.*, **43**, 776-821 (1983).
- Feigenbaum, M. J., "Universal behavior in nonlinear systems", in *Universality in Chaos*, P. Cvitanovic (Ed.), Adam Hilger, pp. 49-84 (1984).
- Fultz, D., Long, R. A., Owens, G. V., Bohan, W., Taylor, R., and Weil, J., "Studies of thermal convection in a rotating cylinder with some implications for large-scale atmospheric motions", *Meteorol. Monogr.*, **4**, American Meteorological Society, Boston, Mass., pp. 1-104 (1959).

Ghil, M., and Childress, S., *Topics in Geophysical Fluid Dynamics: Atmospheric Dynamics, Dynamo Theory, and Climate Dynamics*, Springer-Verlag, New York, 485 pp. (1987).

Guckenheimer, J., and Holmes, P., *Nonlinear Oscillations, Dynamical Systems, and Bifurcations of Vector Fields*, Springer-Verlag, New York/Berlin/Heidelberg/Tokyo, 453 pp. (1983).

Hathaway, D. H., and Somerville, R. C. J., "Thermal convection in a rotating shear flow", *Geophys. Astrophys. Fluid Dyn.*, **38**, 43-68 (1987).

Hide, R., "Experiments with rotating fluids", *Quart. J. Roy. Meteorol. Soc.*, **103**, 1-28 (1977).

Kadanoff, L. P., "Roads to chaos", *Physics Today*, **36(12)**, 46-53 (1983).

Krishnamurti, R., "Some further studies on the transition to turbulent convection," *J. Fluid Mech.*, **60**, 285-303 (1973).

Legras, B. and Ghil, M., "Ecoulements atmosphériques stationnaires, périodiques et aperiodiques", *J. Méc. Théor. Appl.*, no. spécial 1983 (2-D turbulence, R. Moreau, ed.), 45-82 (1983).

Libchaber, A., "The onset of weak turbulence: an experimental introduction". In *Turbulence and Predictability in Geophysical Fluid Dynamics and Climate Dynamics*, edited by M. Ghil, R. Benzi, and G. Parisi, North-Holland Publishing, Amsterdam/New York, pp. 18-28 (1985).

Lorenz, E. N., "Deterministic nonperiodic flow", *J. Atmos. Sci.*, **20**, 130-141 (1963a).

Lorenz, E. N., "The mechanics of vacillation," *J. Atmos. Sci.*, **20**, 448-464 (1963b).

Lorenz, E. N., "The local structure of a chaotic attractor in four dimensions", *Physica*, **13D**, 90-104 (1984).



Or, A. C., and Busse, F. H., "Convection in a rotating cylindrical annulus. Part II. Transitions to asymmetric and vacillating flow", *J. Fluid Mech.*, **174**, 313-326 (1986).

Pedlosky, J., "Finite-amplitude baroclinic waves with small dissipation", *J. Atmos. Sci.*, **28**, 587-597 (1971).

Pedlosky, J. and Frenzen, C., "Chaotic and periodic behavior of finite-amplitude baroclinic waves", *J. Atmos. Sci.*, **37**, 1177-1196 (1980).

Pfeffer, R. L., and Chiang, Y., "Two kinds of vacillation in rotating laboratory experiments", *Mon. Wea. Rev.*, **95**, 75-82 (1967).

Ruelle, D. and Takens, F., "On the nature of turbulence", *Commun. Math. Phys.*, **20**, 167-192 (1971).

Urabe, M., *Nonlinear Autonomous Oscillations*, Springer-Verlag, New York (1967).

### Figure Captions

**Figure 1.** Geometrical configuration of the rotating fluid annulus, with sloping top and bottom "lids".

**Figure 2.** Instability thresholds of pure and mixed solutions,  $(B-B_c)/B_c$  as a function of wavenumber  $\alpha$ ;  $P = 1.0$ . a)  $\eta^* = 700$ , b)  $\eta^* = 1500$ , for Solution I; c)  $\eta^* = 700$ , b)  $\eta^* = 1500$ , for Solution II.

**Figure 3.** Bifurcation diagrams for pure (subscript p) and mixed-mode (subscript m) solutions: amplitude variation versus the Rayleigh number  $R$ . a)  $\chi \cong \pm 2\pi/3$ . The points  $R_1$ ,  $P_u$ ,  $R_u$ , and  $Q_u^I$  in  $(A, R)$  coordinates here are associated with the same points given in  $(B, \alpha)$  coordinates in Figures 2a,b. b)  $\chi \cong \pm \pi/12$ . Points  $R_1'$  and  $Q_u^{II}$  correspond to those in Figures 2c,d. Solid lines represent stable solutions and dashed lines represent unstable solutions. In both panels  $\eta^* = 700$ , and the bifurcation structure persists for all  $\alpha > \alpha_c$  we investigated (compare Figures 2 and 8).

**Figure 4.** Neutral mixed-mode stability curve  $N = 0$  for Solution I (solid) and for Solution II (dashed) in the  $\eta^* - P$  parameter plane, at critical values  $B_c$  and  $\alpha_c$ .

**Figure 5.** Successive bifurcations in Solution I and in the first unsteady band of Solution II.

**Figure 6.** Solution structure in the  $B - \eta^*$  (buoyancy-Coriolis) plane. a) Solution I; b) Solution II.  $P = 1.0$ ,  $\alpha = \alpha_c = 9.37$ .

**Figure 7.** Frequency dependence on buoyancy parameter for Solutions I and II.  $\eta^* = 700$ ,  $P = 1$ ,  $\alpha = \alpha_c$ .

**Figure 8.** Mean-flow and vacillating instability boundaries, as a function of wavenumber;  $\eta^* = 700$ . a)  $P = 0.3$ , b)  $P = 1.0$ ; c) This panel is the same as panel (a), except it is calculated by the model of OB86, d) Same as panel (b), except as calculated by the model of OB86.

**Figure 9.** Marginal stability curves for the mean-flow and vacillating flow regimes as a function of  $B$  vs.  $P$  at the critical wavenumber  $\alpha = \alpha_c$ , and at  $\eta^* = 700$ . a) Solution I; b) Solution II.

**Figure 10.** The absolute amplitudes of the first (solid) and second (dashed) modes of the streamfunction for Solution II, as a function of time. a) The variation as calculated by a Runge-Kutta method; b) Fourier-decomposition method.  $B = 38893$ ,  $\eta^* = 700$ ,  $P = 1$ ,  $\alpha = \alpha_c$ ,  $c = 12.7$ .

**Figure 11.** The power spectrum of Solution II in two cases: (a,c)  $B = 38893$ , simply-periodic solution; (b,d)  $B = 39156$ , after period doubling. The solution was calculated by a Runge-Kutta method (a,b) and by Fourier decomposition (c,d), respectively.  $P = 1.0$ ,  $\eta^* = 700$ ,  $\alpha = \alpha_c$ . The two lines correspond to the spectrum of the two modes, with the first mode having more power than the second at all frequencies.

**Figure 12.** Solution II: streamfunction amplitudes of modes 1 (solid) and 2 (dashed) as functions of time;  $\eta^* = 700$ ,  $\alpha = \alpha_c$ . a)  $B = 38893$ , b)  $B = 40000$ , c)  $B = 40355$ , d)  $B = 40380$ .

**Figure 13.** Phase plane of kinetic energy (change in kinetic energy versus kinetic energy);  $P = 1.0$ ,  $\eta^* = 700$ ,  $\alpha = \alpha_c$ . a) Solution I : i)  $B = 38893$ , ii)  $B = 39240$ , iii)  $B = 39645$ , iv)  $B = 39704$ , v)  $B = 39720$ ; b) Solution II: i)  $B = 36500$ , ii)  $B = 38893$ , iii)  $B = 40000$ , iv)  $B = 40350$ , v)  $B = 40367$ , vi)  $B = 40375$ .

**Figure 14.** Velocity phase plane,  $v$  vs.  $u$ . Panels (i)-(v) in Figure 14a correspond to those in Figure 13a, and (i)-(vi) in Figure 14b to Figure 13b.

**Figure 15.** Poincaré maps  $A$  vs.  $B$ . Maps (i)-(v) in Figure 15a correspond to those in Figure 13a and (i)-(vi) in Figure 15b to Figure 13b.

**Figure 16.** Time evolution of the streamfunction field through one full period, for  $B = 38893$ ,  $\eta^* = 700$ ,  $P = 1.0$ ,  $\alpha = \alpha_c$ , and  $c = 0$ . a) Solution I; b) Solution II.

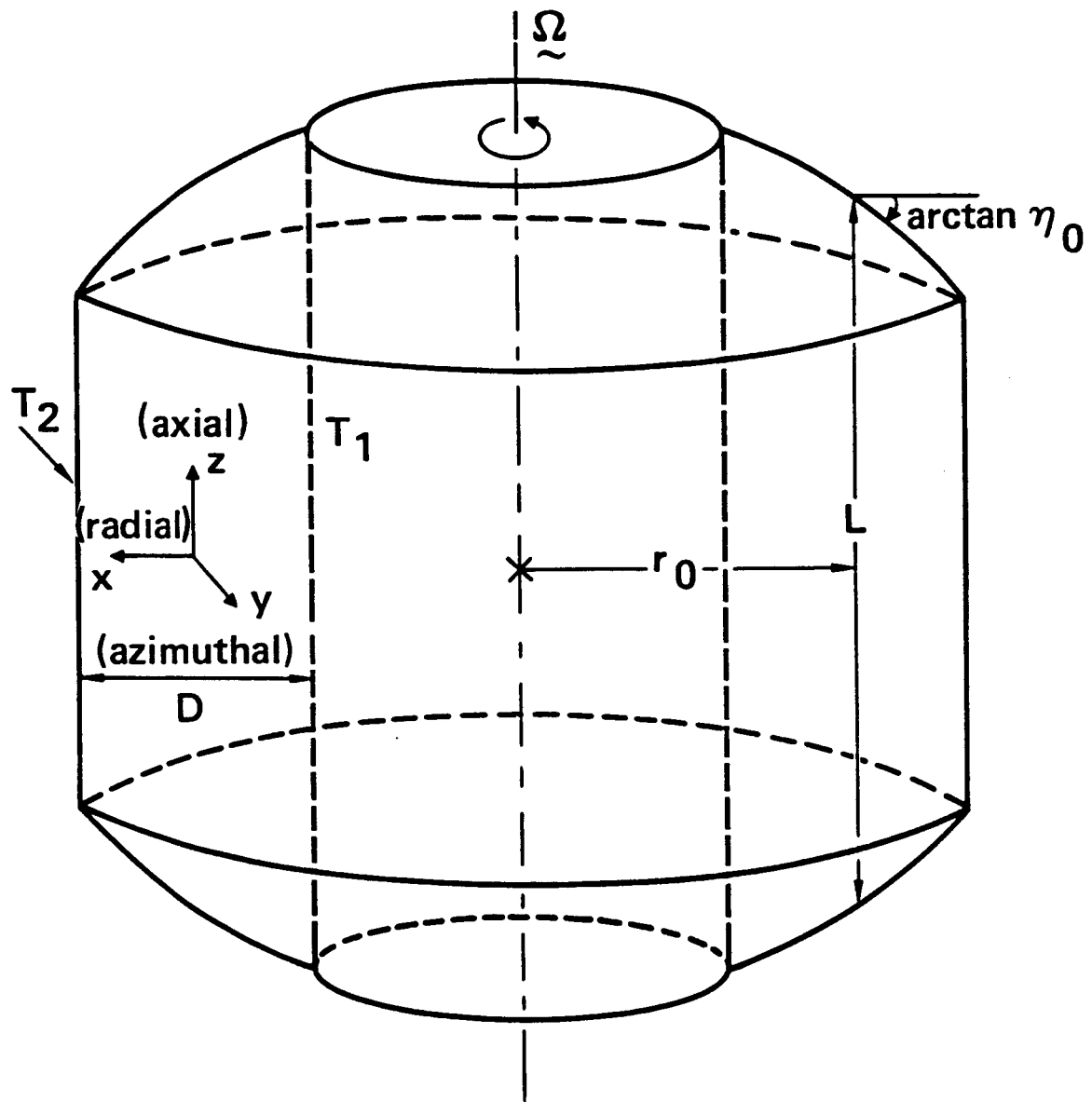


Fig. 1

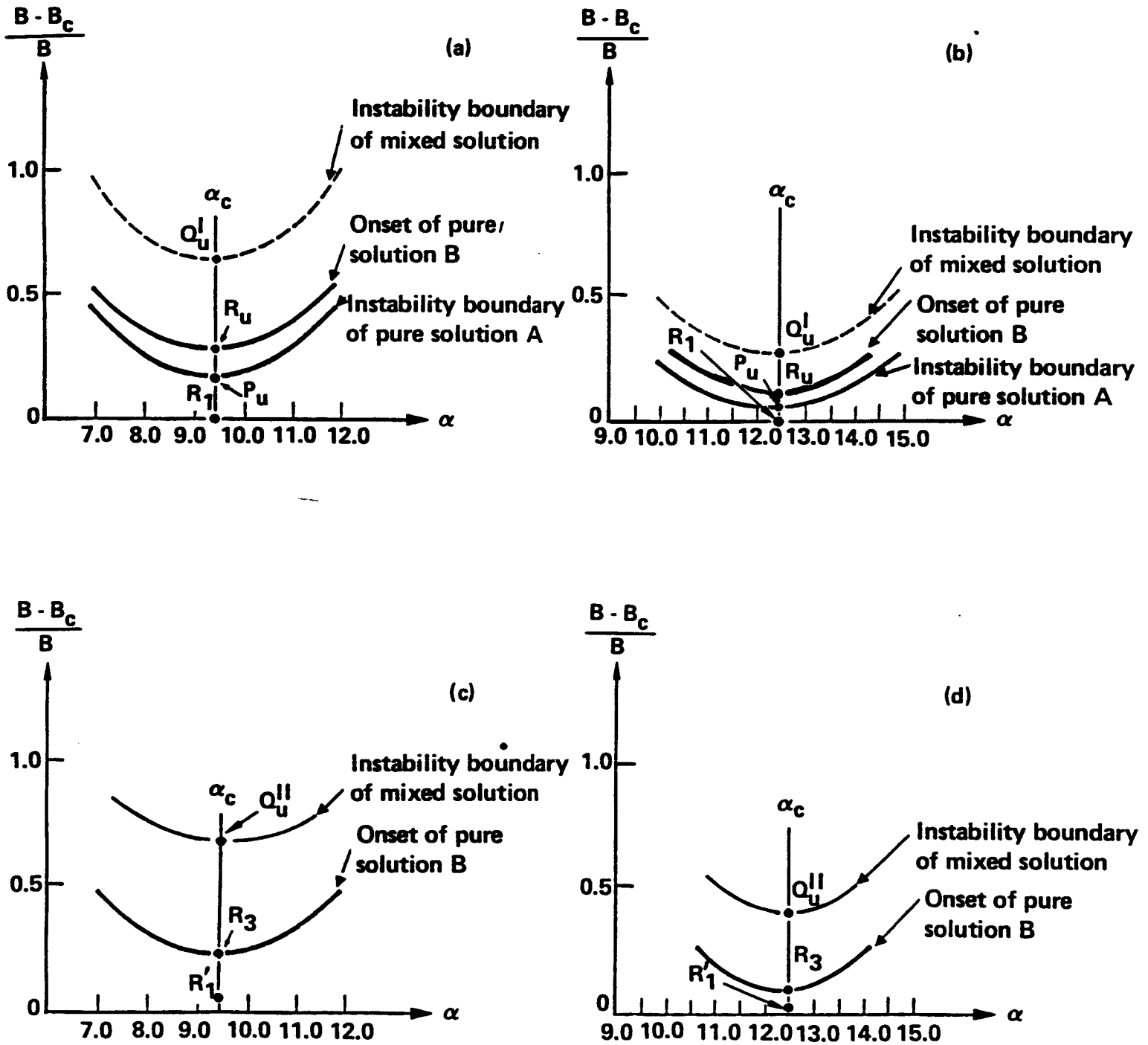


Fig. 2

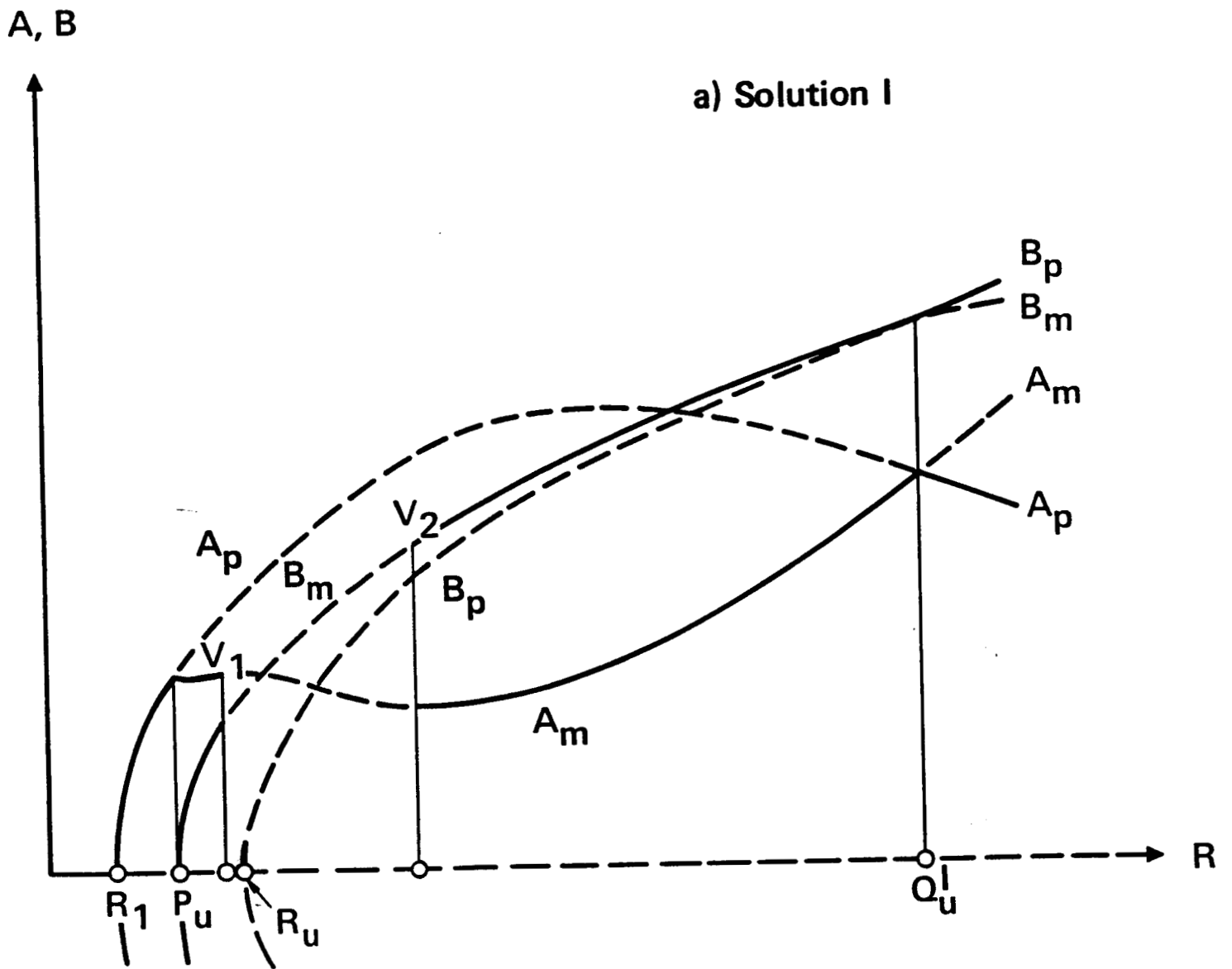


Fig. 3a

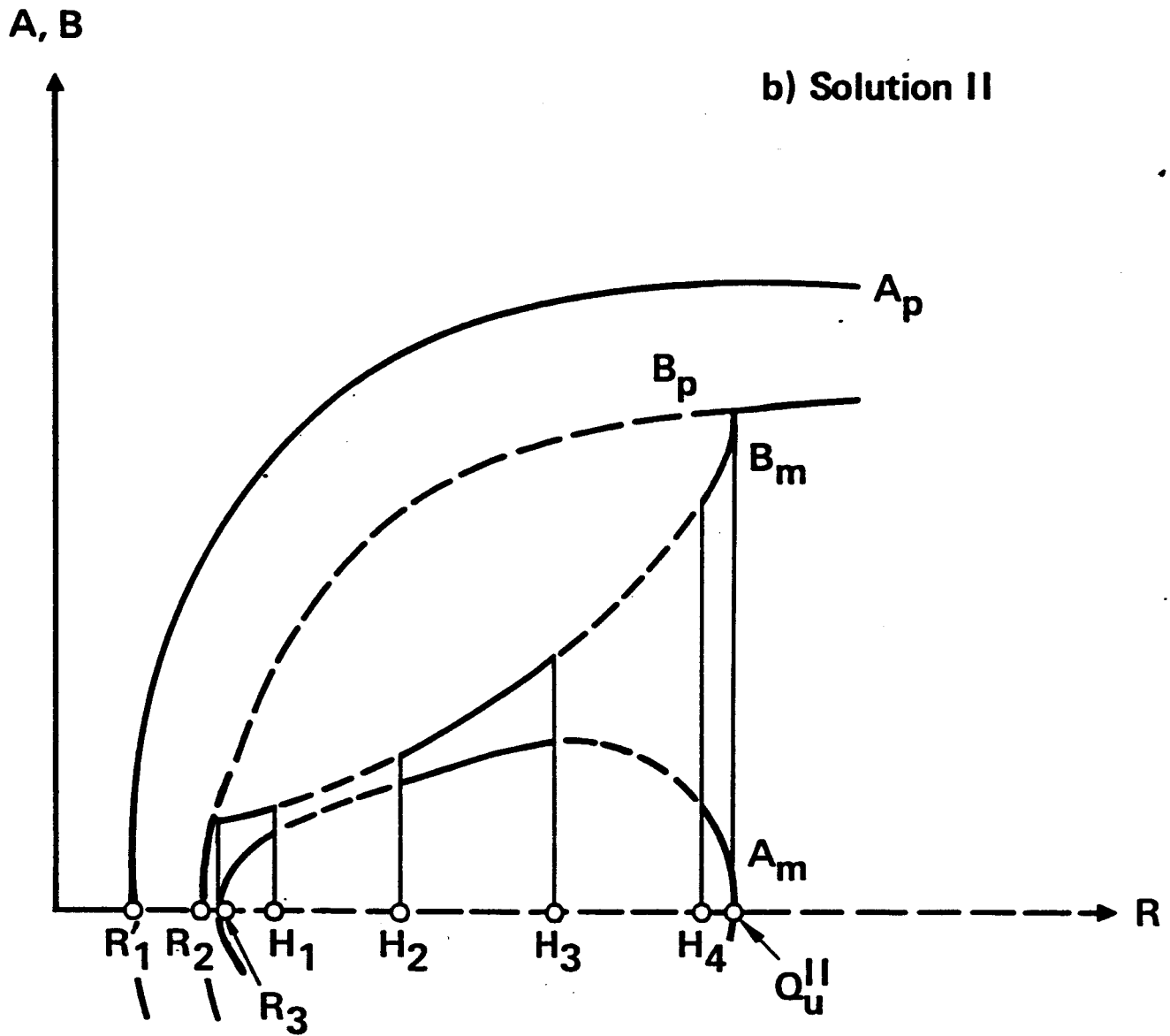


Fig. 3b

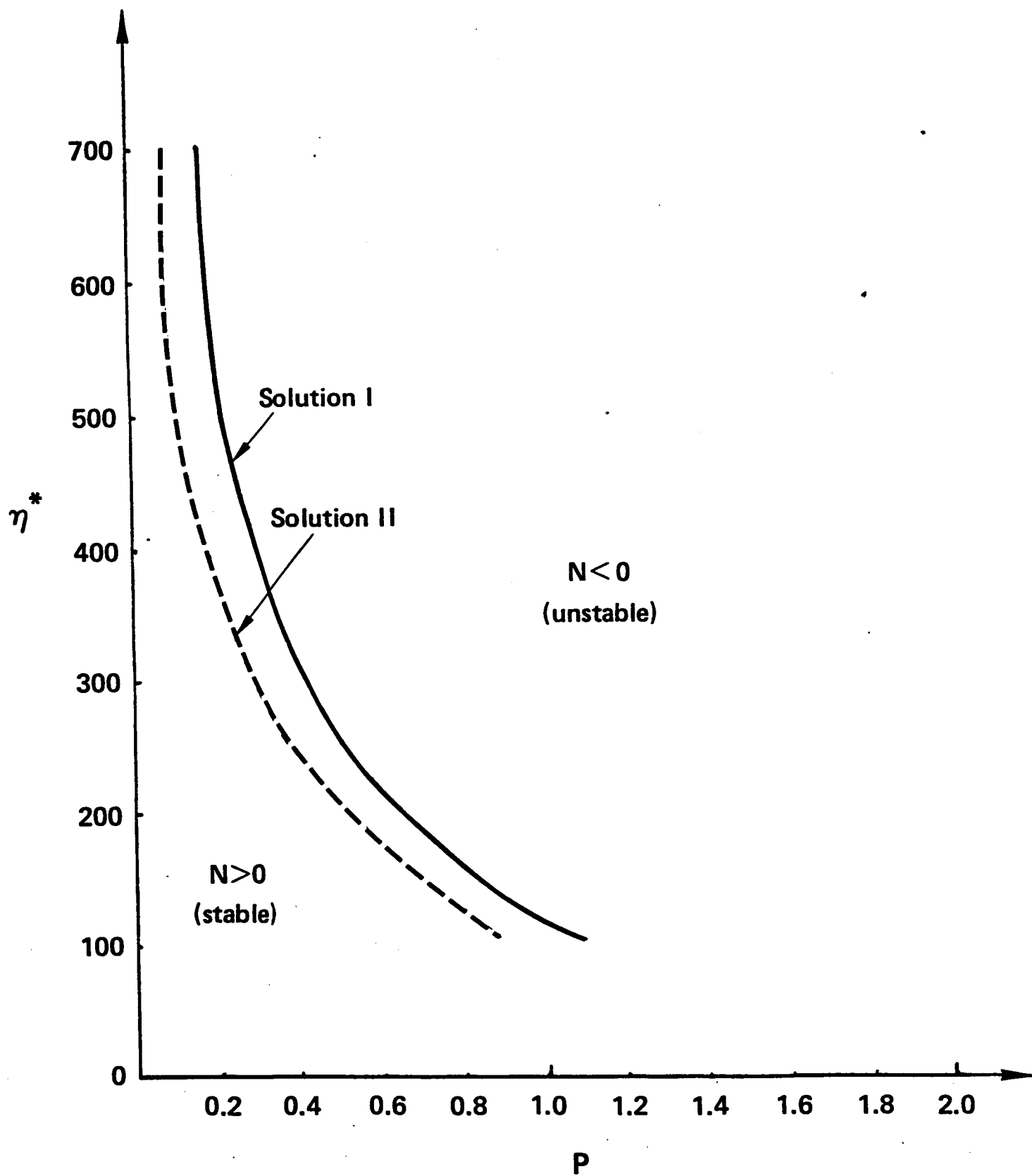


Fig. 4



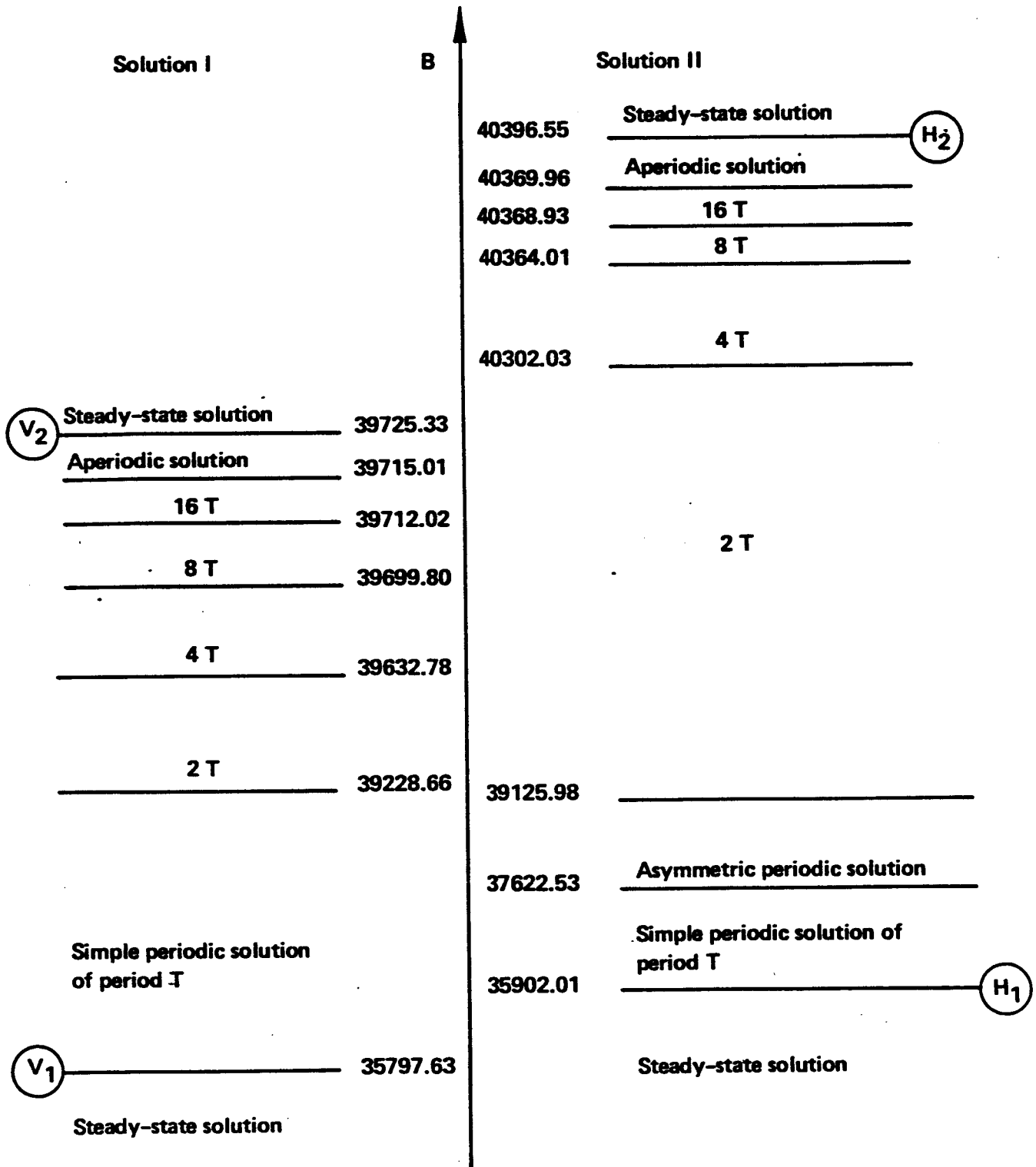


Fig. 5

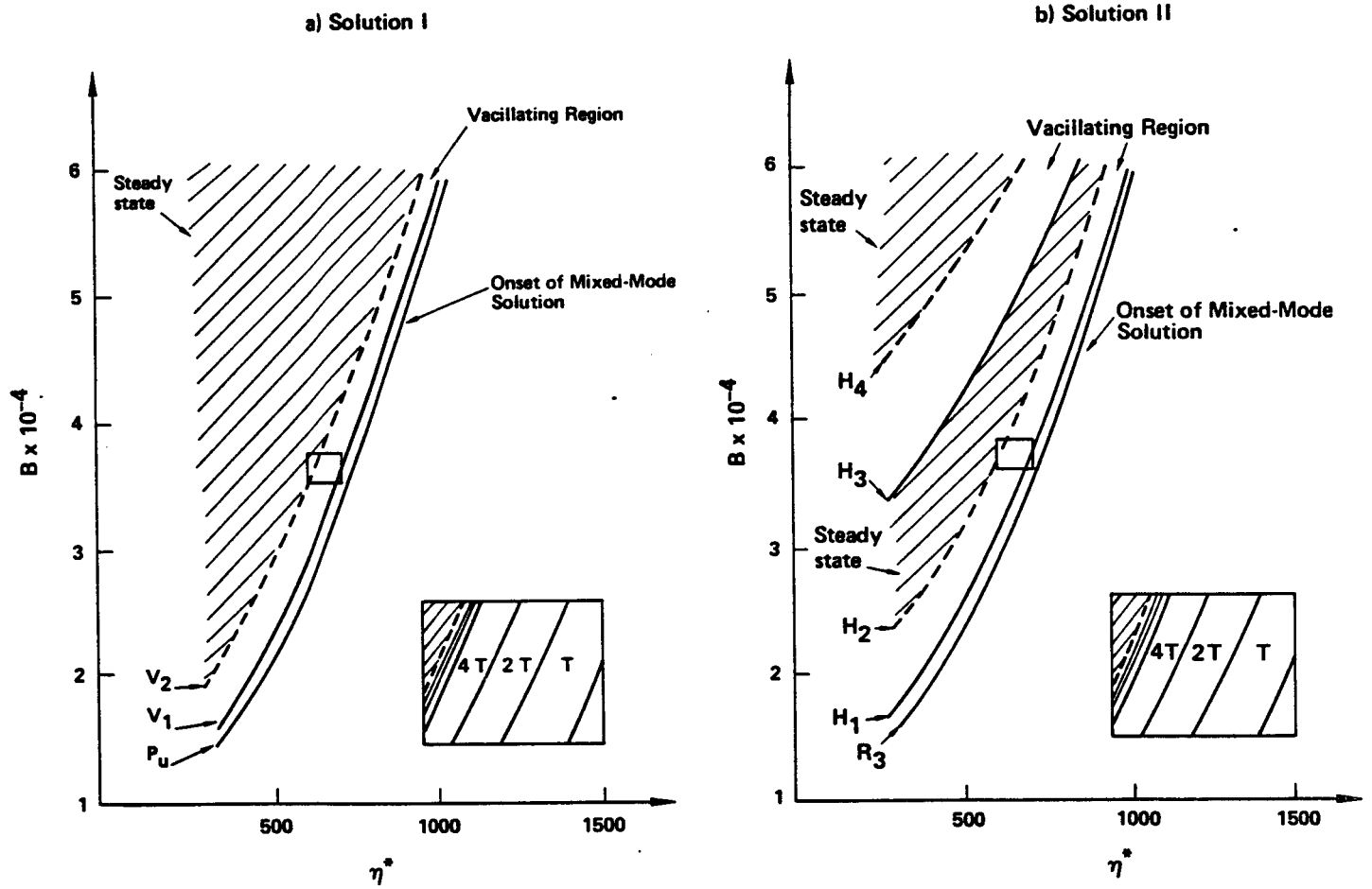


Fig. 6

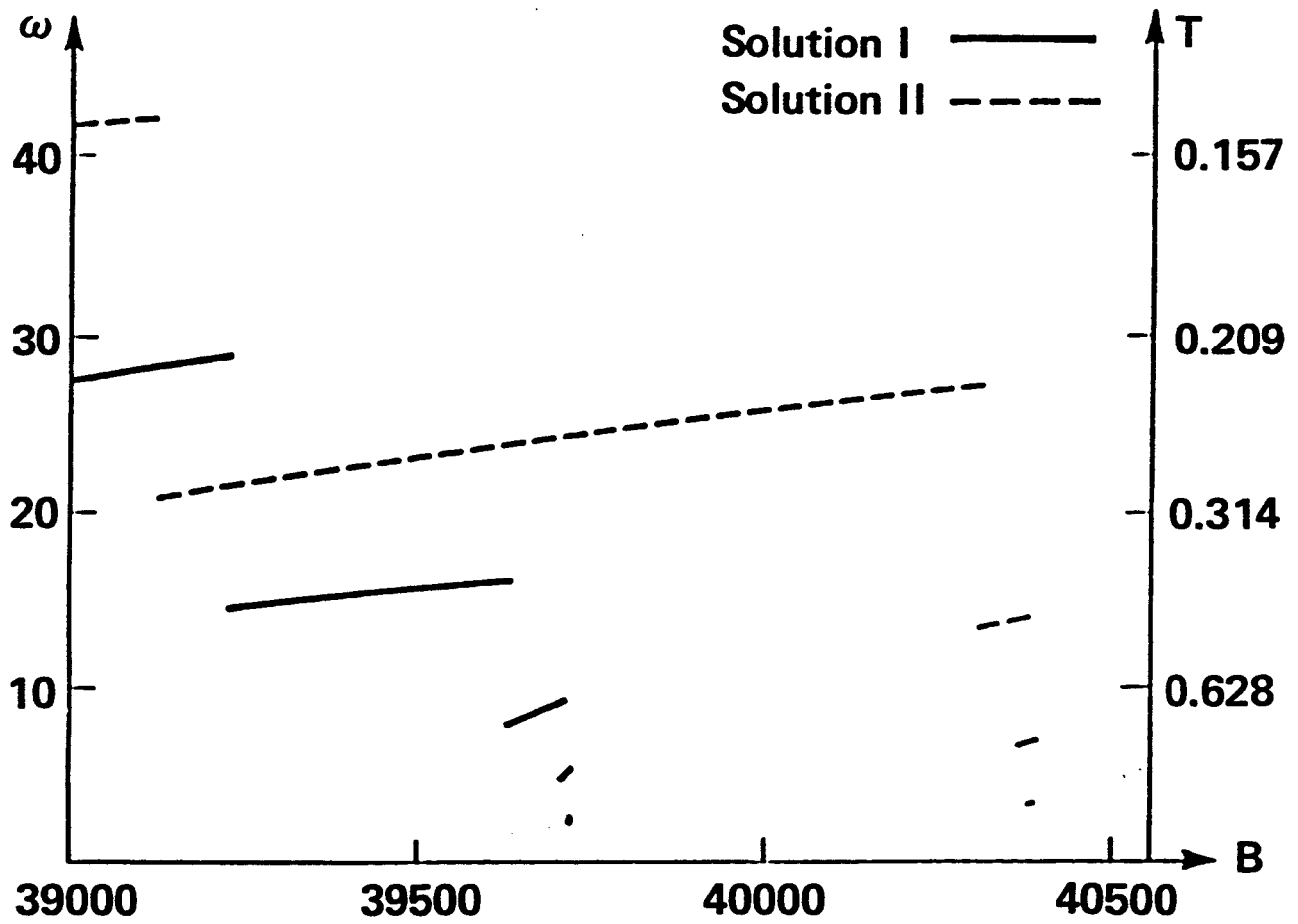


Fig. 7

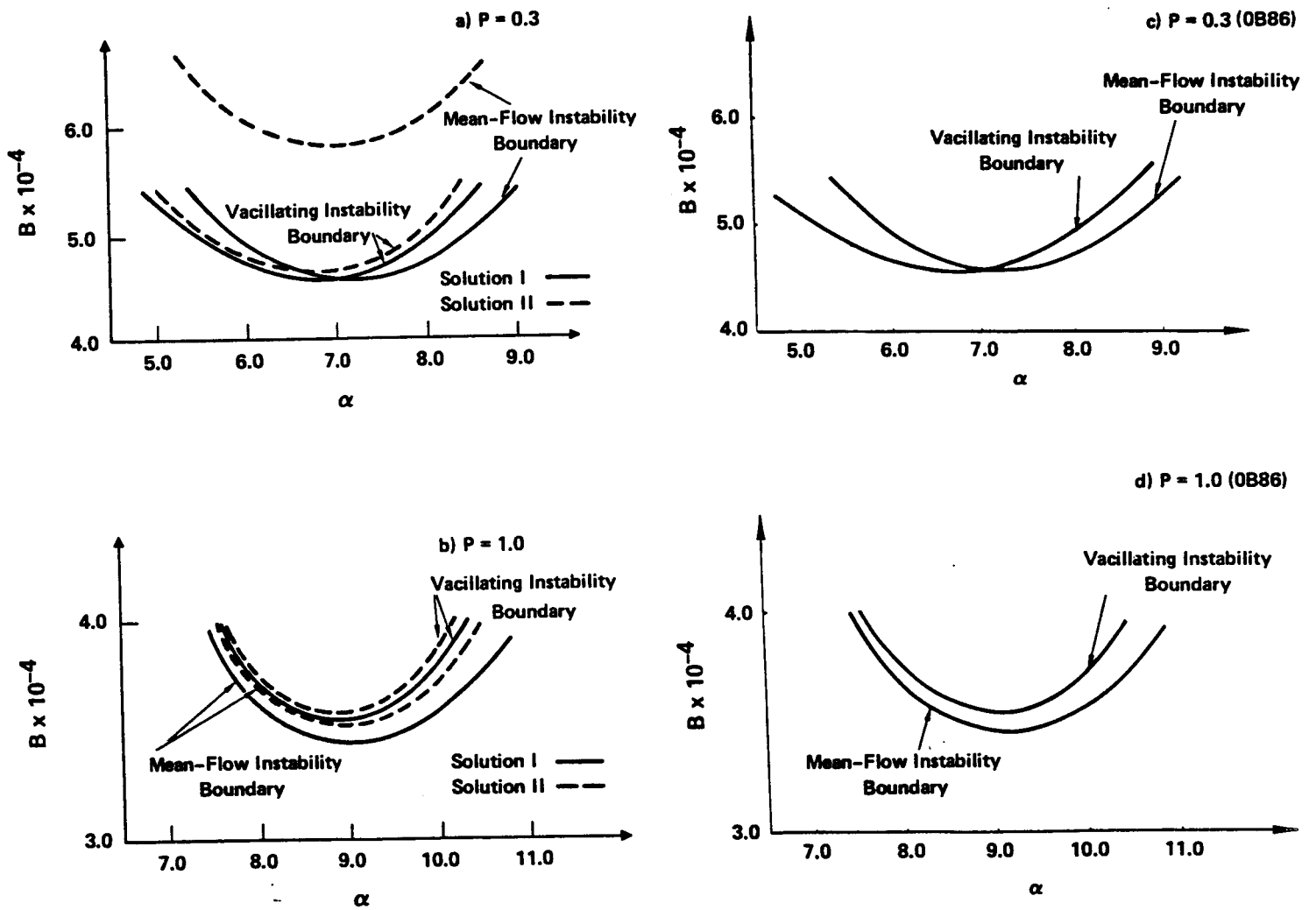


Fig. 8

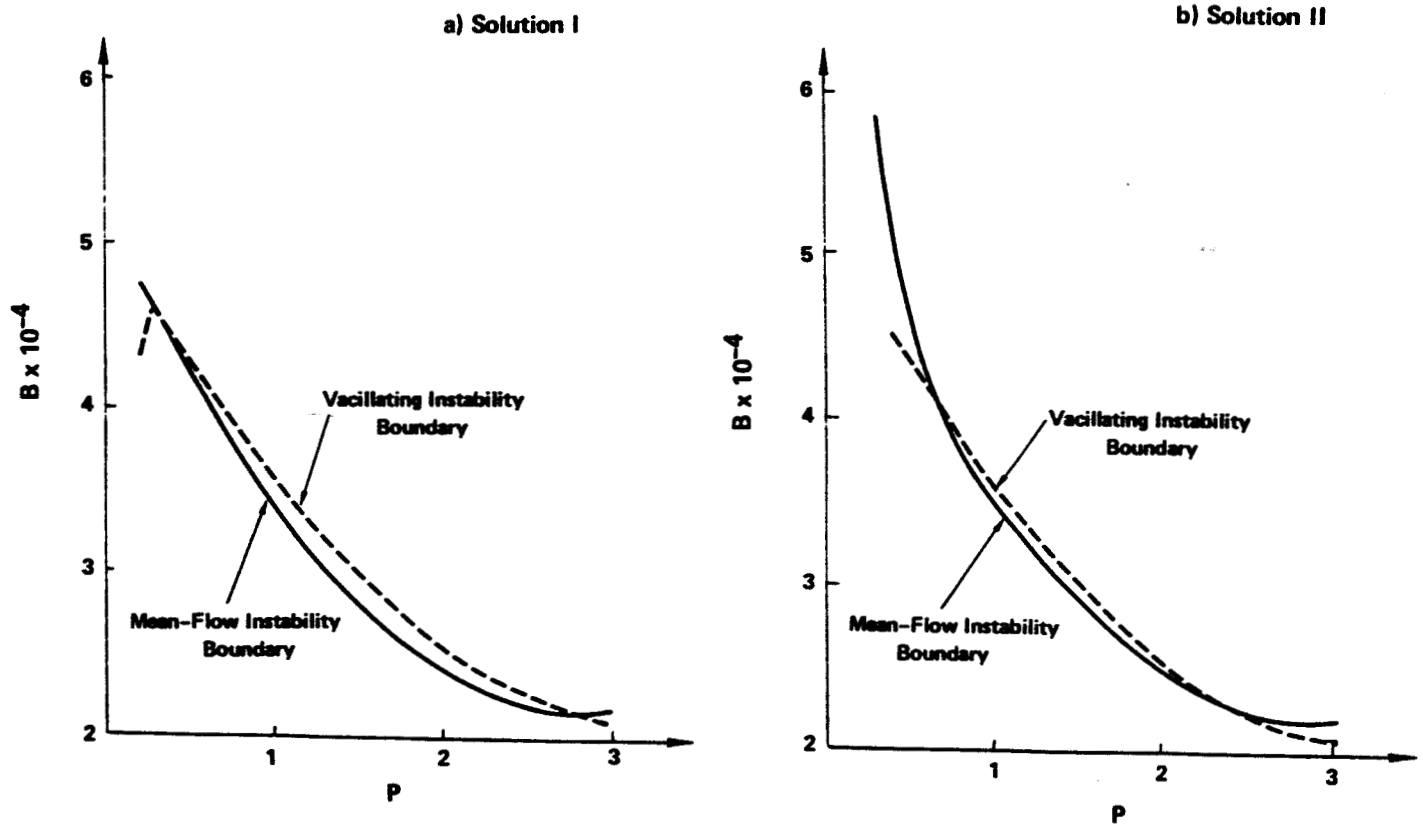


Fig. 9

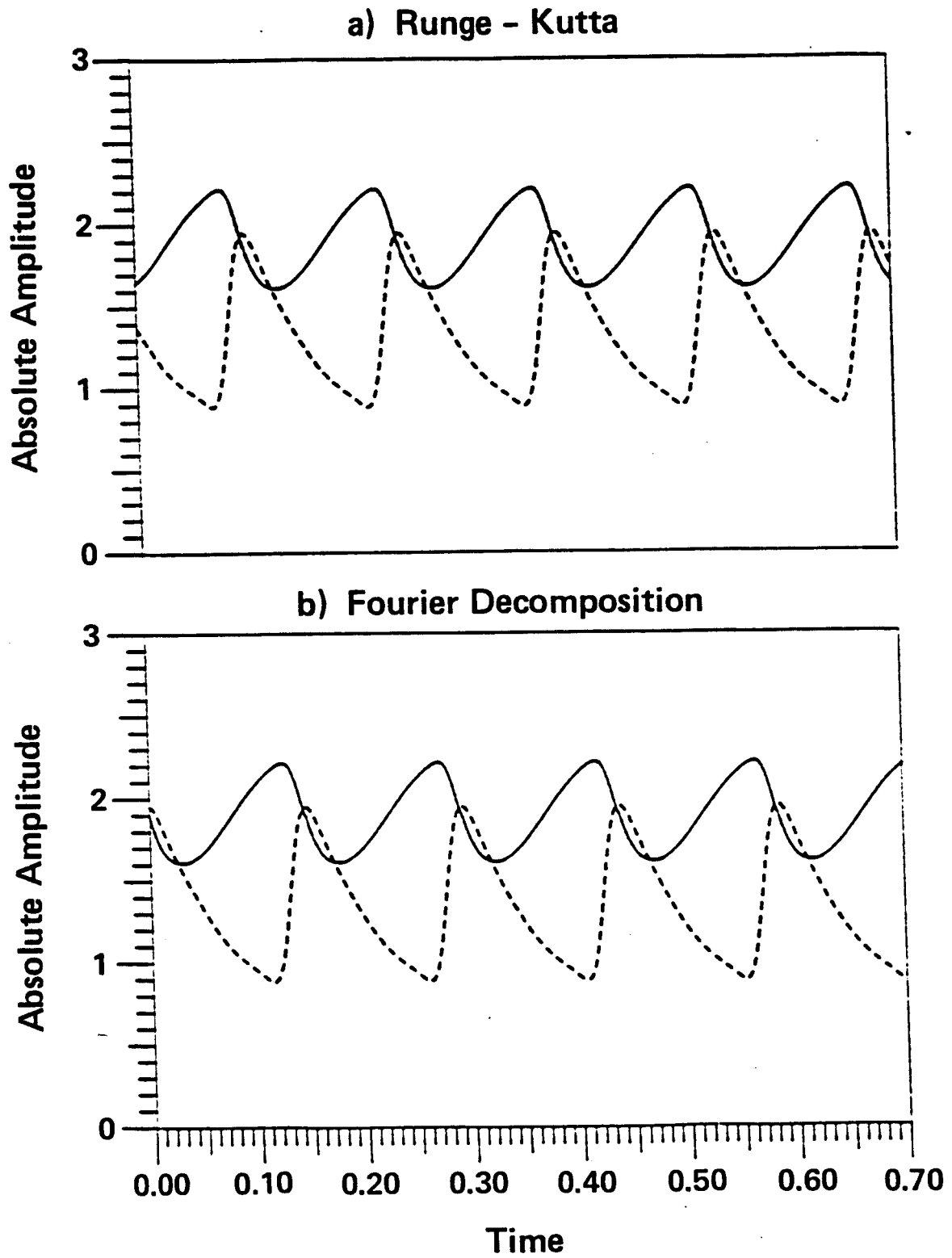
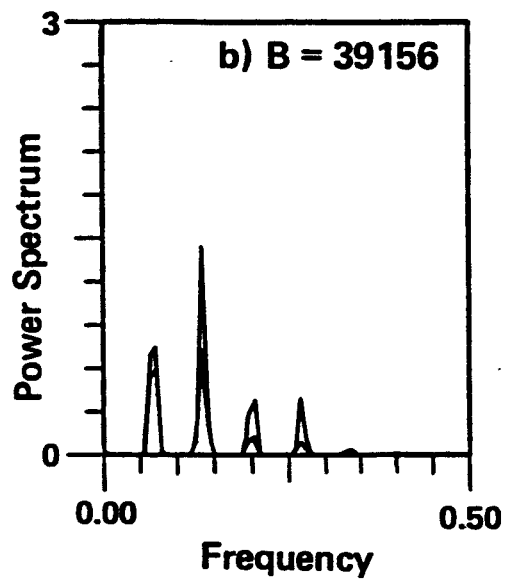
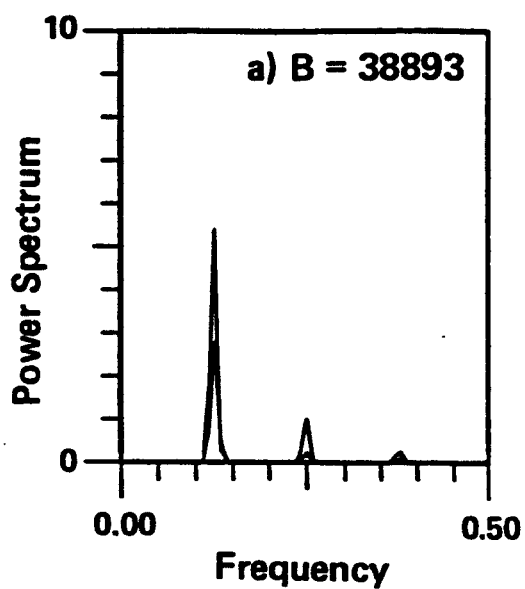


Fig. 10

Runge-Kutta (a, b)



Fourier Decomposition (c, d)

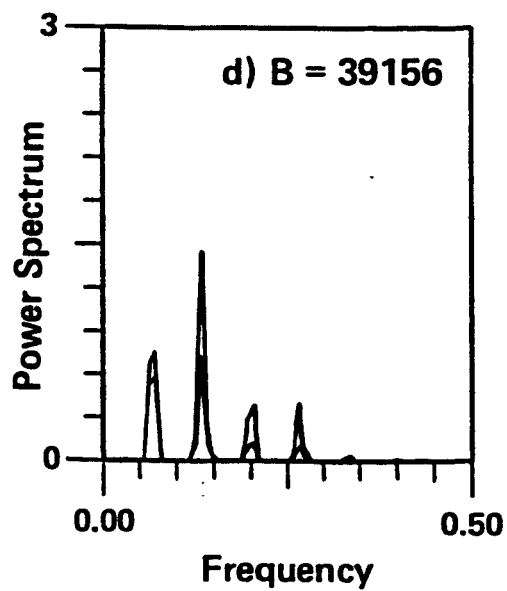
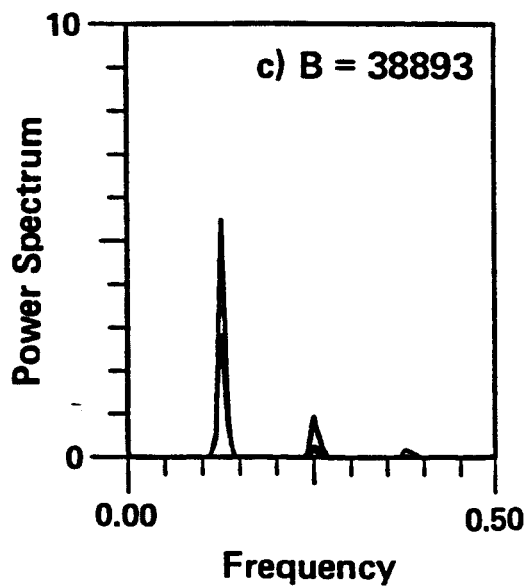


Fig. 11

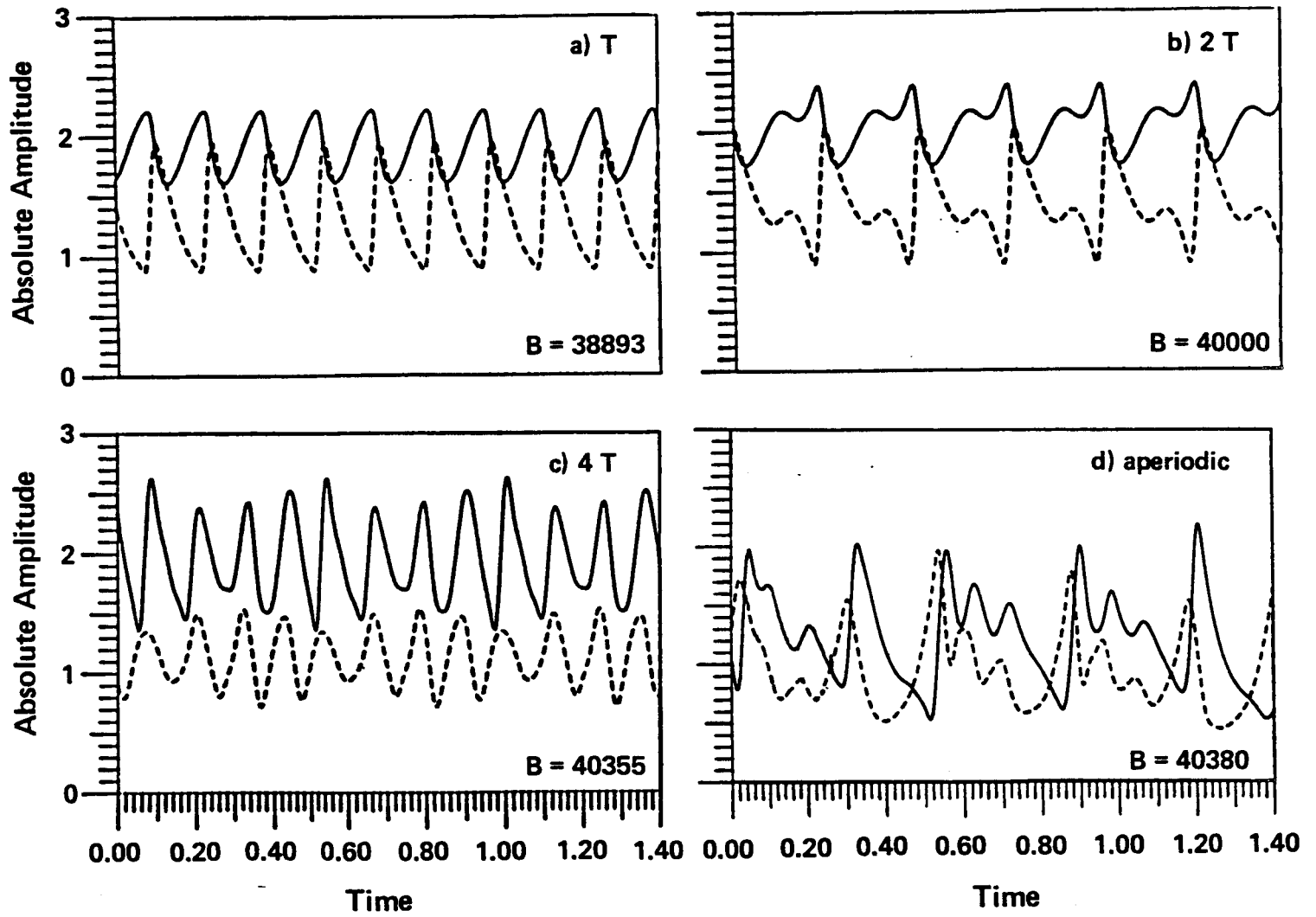


Fig. 12



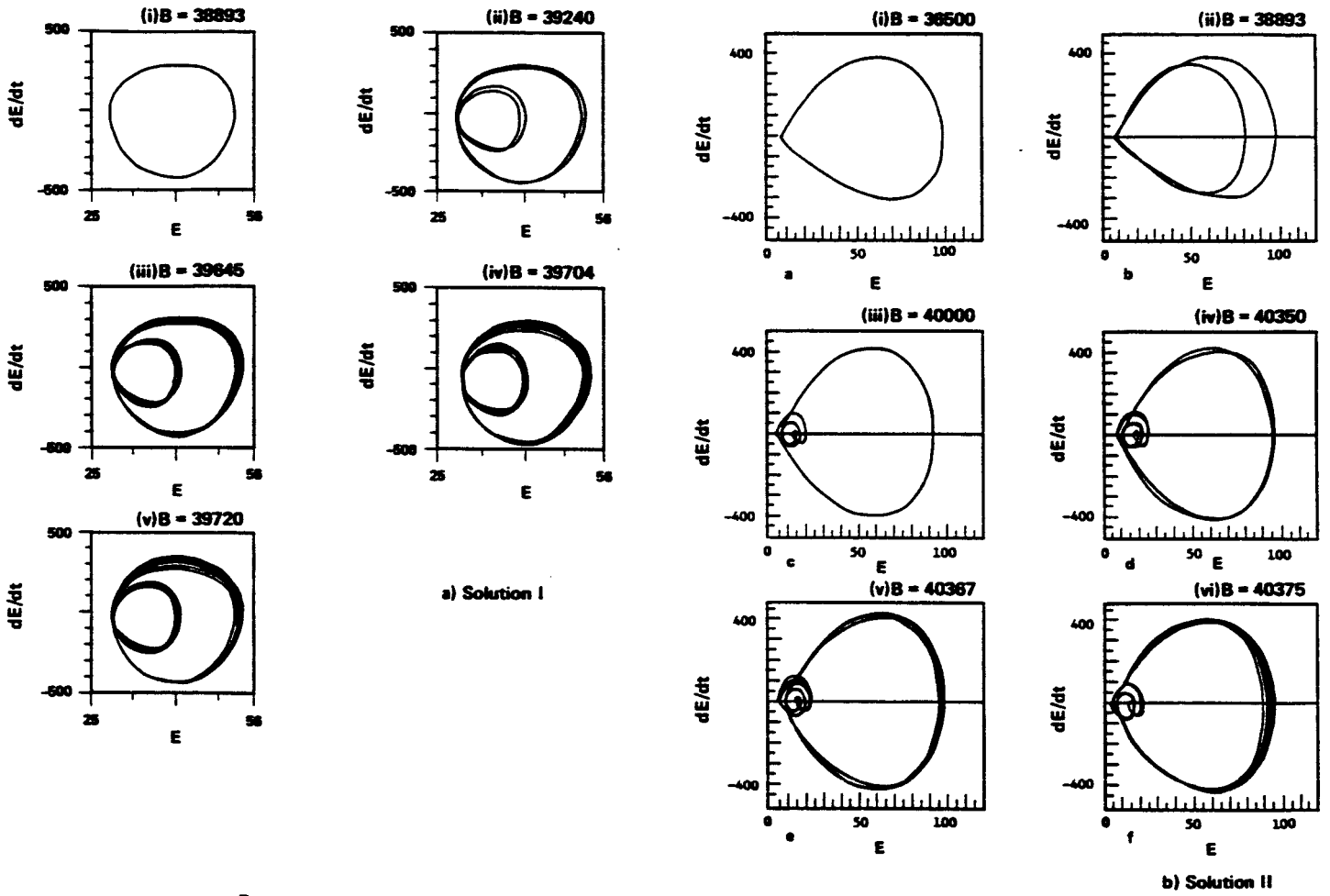
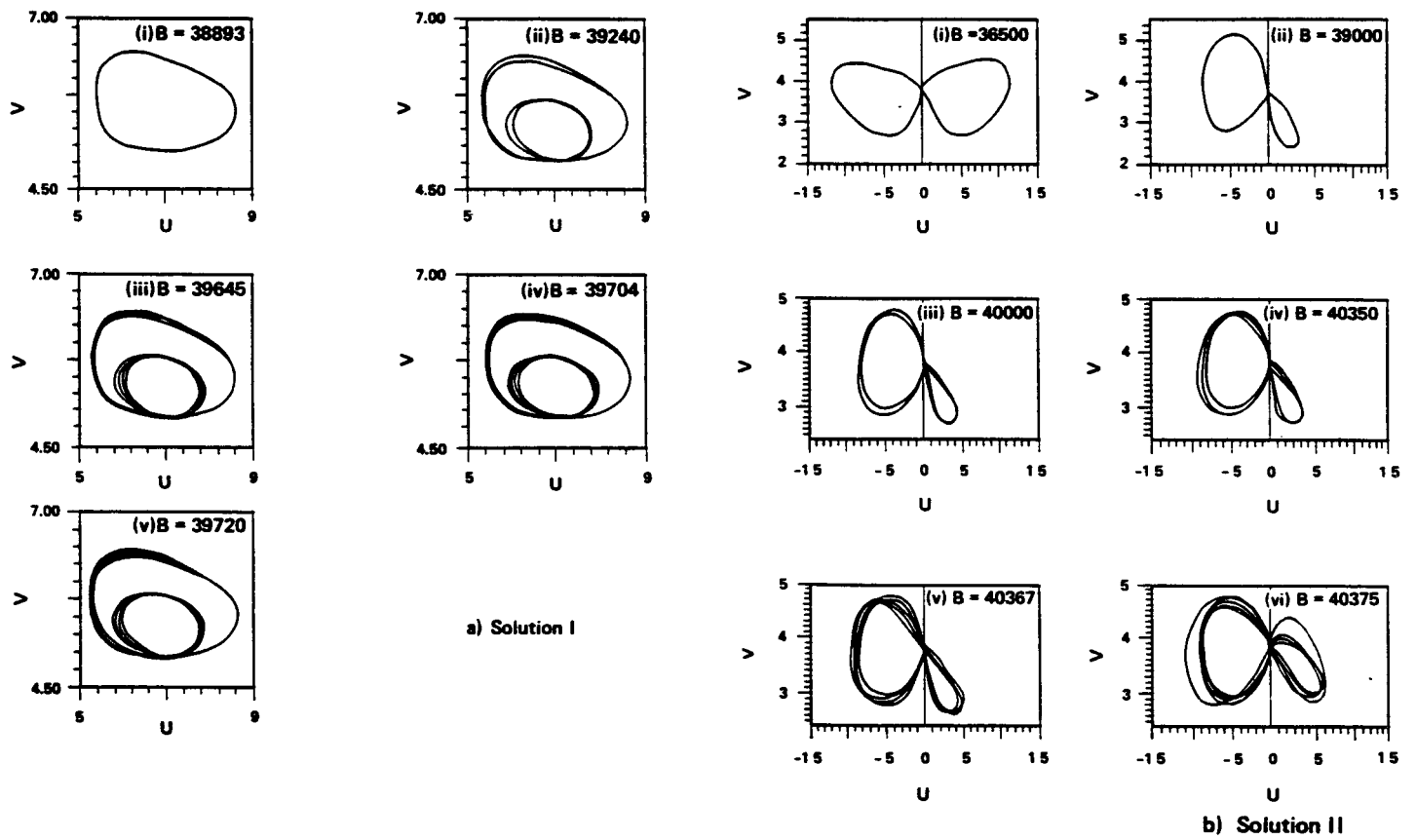


Fig. 13



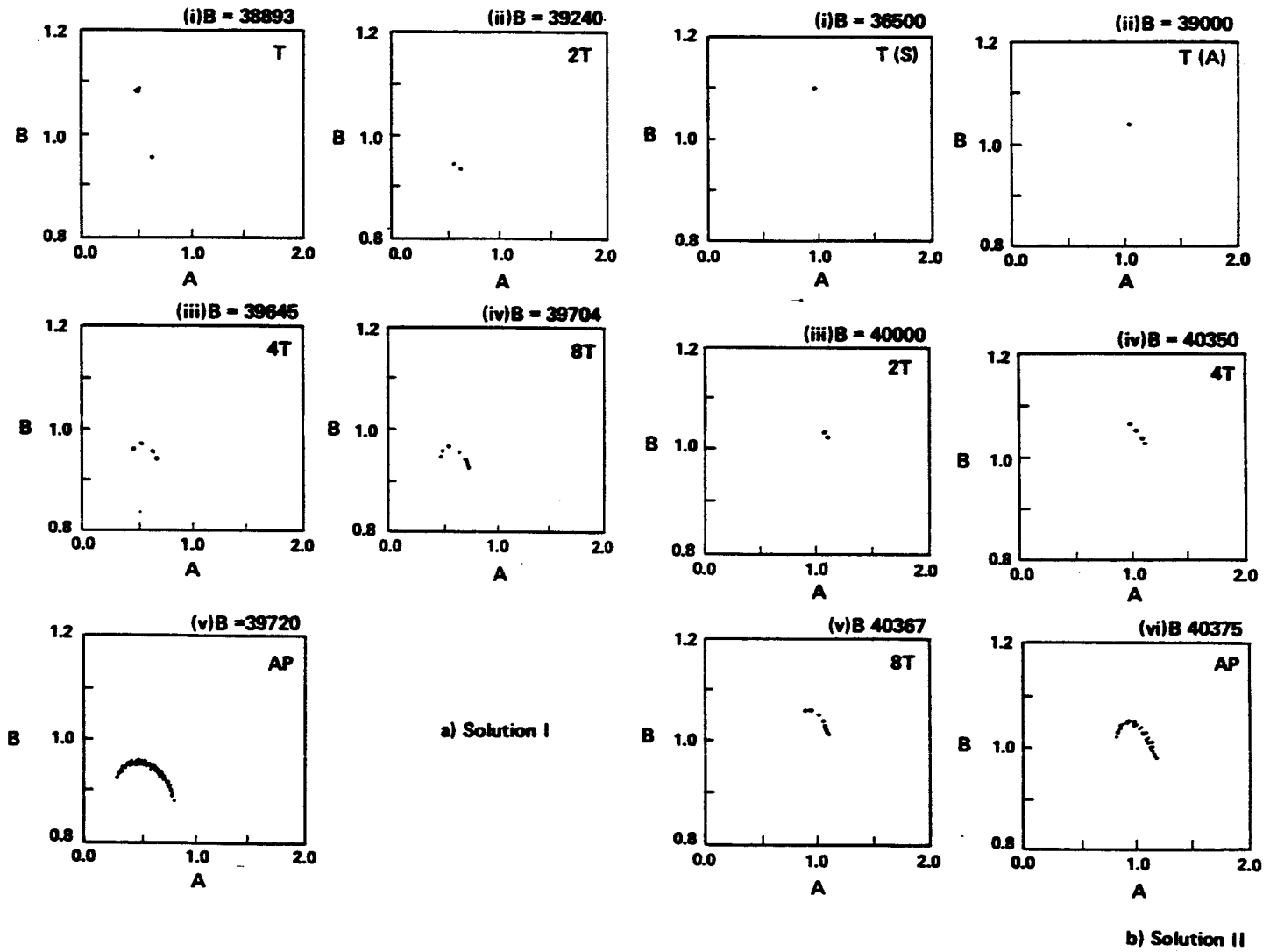
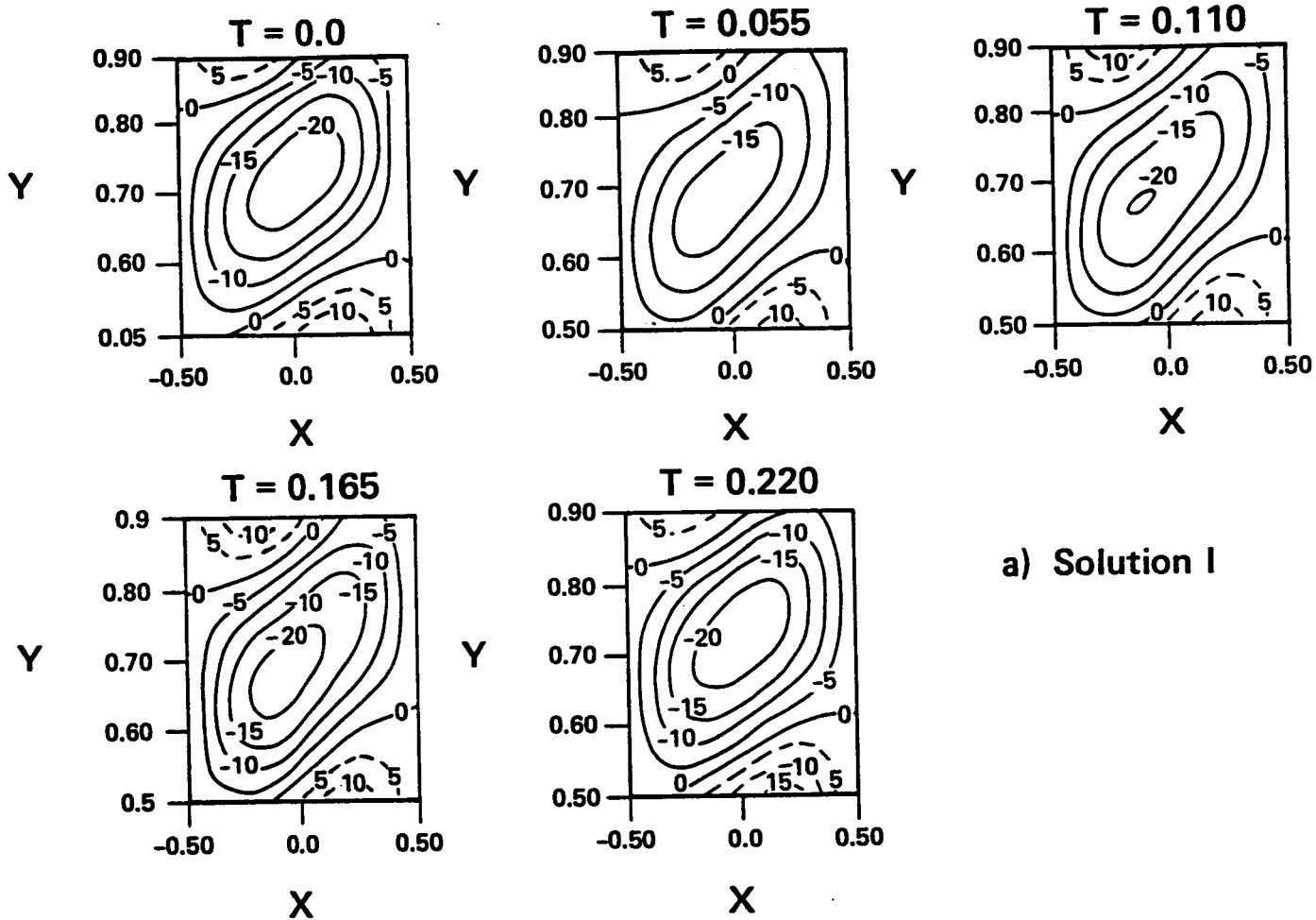


Fig. 15



a) Solution I

Fig. 16a

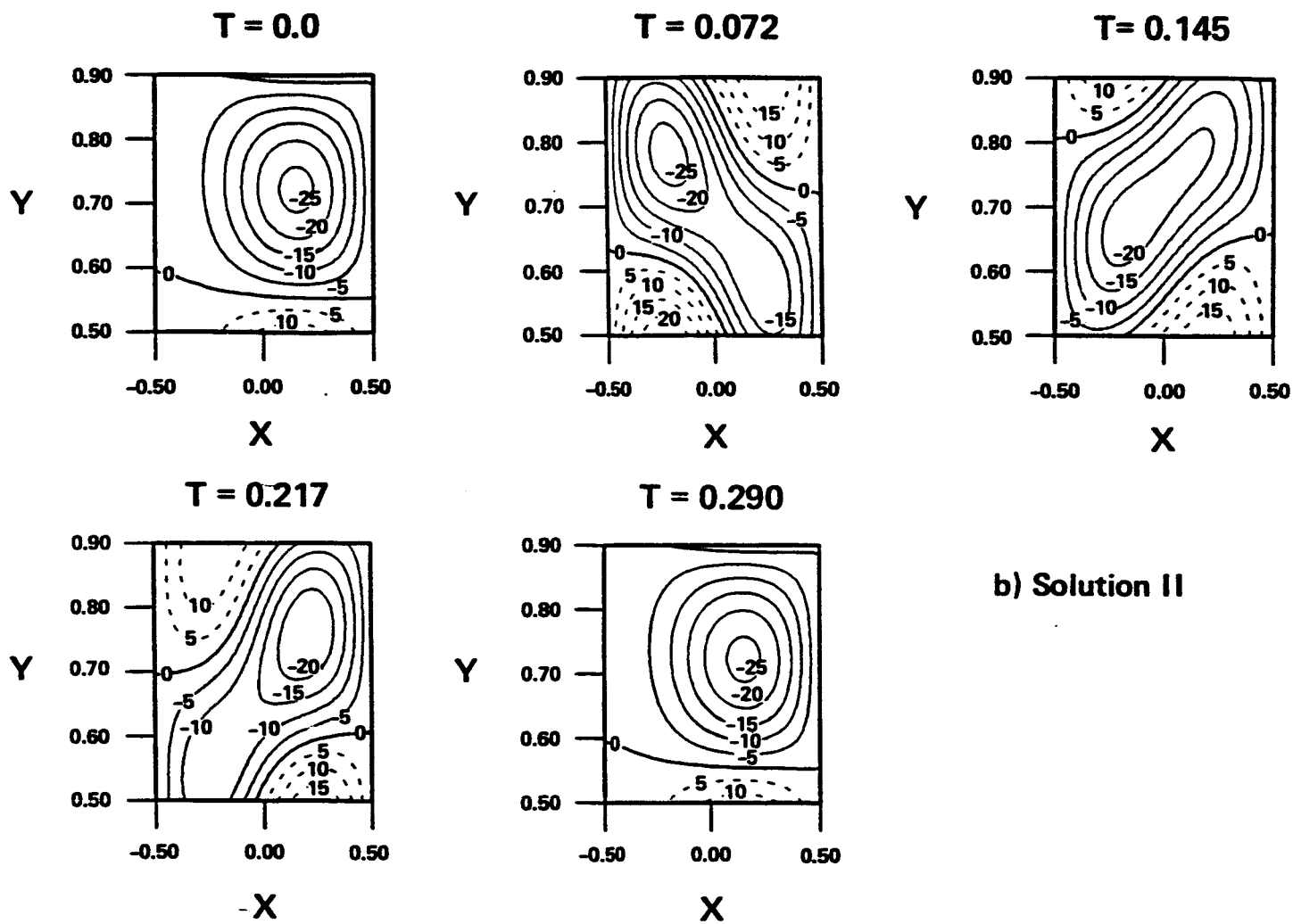


Fig. 16b